









Strain-stabilized superconductivity

J. P. Ruf ¹✉, H. Paik^{2,3}, N. J. Schreiber³, H. P. Nair³, L. Miao¹, J. K. Kawasaki ^{1,4}, J. N. Nelson ¹, B. D. Faeth^{1,2}, Y. Lee¹, B. H. Goodge ^{5,6}, B. Pamuk⁵, C. J. Fennie ⁵, L. F. Kourkoutis ^{5,6}, D. G. Schlom ^{3,6,7} & K. M. Shen ^{1,6}✉

Superconductivity is among the most fascinating and well-studied quantum states of matter. Despite over 100 years of research, a detailed understanding of how features of the normal-state electronic structure determine superconducting properties has remained elusive. For instance, the ability to deterministically enhance the superconducting transition temperature by design, rather than by serendipity, has been a long sought-after goal in condensed matter physics and materials science, but achieving this objective may require new tools, techniques and approaches. Here, we report the transmutation of a normal metal into a superconductor through the application of epitaxial strain. We demonstrate that synthesizing RuO₂ thin films on (110)-oriented TiO₂ substrates enhances the density of states near the Fermi level, which stabilizes superconductivity under strain, and suggests that a promising strategy to create new transition-metal superconductors is to apply judiciously chosen anisotropic strains that redistribute carriers within the low-energy manifold of *d* orbitals.

¹Department of Physics, Laboratory of Atomic and Solid State Physics, Cornell University, Ithaca, NY 14853, USA. ²Platform for the Accelerated Realization, Analysis, and Discovery of Interface Materials, Cornell University, Ithaca, NY 14853, USA. ³Department of Materials Science and Engineering, Cornell University, Ithaca, NY 14853, USA. ⁴Department of Materials Science and Engineering, University of Wisconsin, Madison, WI 53706, USA. ⁵School of Applied and Engineering Physics, Cornell University, Ithaca, NY 14853, USA. ⁶Kavli Institute at Cornell for Nanoscale Science, Ithaca, NY 14853, USA. ⁷Leibniz-Institut für Kristallzüchtung, Max-Born-Str. 2, Berlin 12489, Germany. ✉email: jpr239@cornell.edu; kmshen@cornell.edu

In typical weak-coupling theories of superconductivity, the effective attraction V between electrons is mediated by the exchange of bosons having a characteristic energy scale ω_B , and superconductivity condenses below a transition temperature T_c parameterized as¹:

$$T_c \sim \omega_B \exp\left(-\frac{1}{N(E_F)V}\right) = \omega_B \exp\left(-\frac{1+\lambda}{\lambda-\mu^*}\right), \quad (1)$$

where $N(E_F)$ is the density of states (DOS) near the Fermi level, λ is the electron–boson coupling strength, and μ^* is the Coulomb pseudopotential that describes the residual Coulomb repulsion between quasiparticles². For simplicity, we assume that all of the non-isotropic \mathbf{q} - and \mathbf{k} -dependencies that appear in a more realistic formulation of Cooper pairing have been averaged away. Note that within the range of validity of Eq. (1)—viz., $1 \gg \lambda > \mu^*$ —increasing λ (increasing μ^*) generally enhances (suppresses) T_c , respectively, assuming that superconductivity remains the dominant instability.

Experimental methods that boost T_c are highly desired from a practical perspective. Furthermore, by analyzing how these available knobs couple to the normal-state properties on the right side of Eq. (1), one can envisage engineering the electronic structure and electron–boson coupling to optimize T_c . For example, increasing $N(E_F)$ is a frequently suggested route towards realizing higher T_c , but how to achieve this for specific materials often remains unclear.

Historically, chemical doping and hydrostatic pressure have been the most common knobs used to manipulate superconductivity. Unfortunately, doping has the complication of explicitly introducing substitutional disorder, whereas pressure studies are incompatible with most probes of electronic structure. Moreover, because large pressures are usually required to appreciably increase T_c ³, pressure-enhanced superconductivity exists transiently—oftentimes in different structural polymorphs than at ambient conditions—rendering it inaccessible for applications.

An alternative strategy for controlling superconductivity is epitaxial strain engineering. This approach is static, disorder-free, allows for the use of sophisticated experimental probes⁴, and enables integration with other materials in novel artificial interfaces and device structures^{5,6}. To date, epitaxial strain has only been used to modulate T_c in known superconductors^{7–12}. In this article, we describe the creation of a new superconductor through epitaxial strain, starting from a compound, RuO₂, previously not known to be superconducting. By comparing the results of angle-resolved photoemission spectroscopy (ARPES) experiments with density functional theory (DFT) calculations, we show that splittings between the effective low-energy d orbital degrees of freedom in RuO₂ respond sensitively to appropriate modes of strain, and we discuss how this approach may open the door to strain tuning of superconductivity in other materials.

Results

Electrical and structural characterization of RuO₂ thin films.

Bulk RuO₂ crystallizes in the ideal tetragonal rutile structure (space group #136, $P4_2/mnm$) with lattice constants at 295 K of ($a = 4.492 \text{ \AA}$, $c = 3.106 \text{ \AA}$)¹³. RuO₂ thin films in distinct epitaxial strain states were synthesized using oxide molecular-beam epitaxy (MBE) by employing different orientations of isostructural TiO₂ substrates, ($a = 4.594 \text{ \AA}$, $c = 2.959 \text{ \AA}$)¹⁴. As shown in Fig. 1a, b, the surfaces of (101)-oriented substrates are spanned by the $[\bar{1}01]$ and $[010]$ lattice vectors of TiO₂, which ideally impart in-plane tensile strains on RuO₂ (at 295 K) of +0.04% and +2.3%, respectively. On TiO₂(110), the lattice mismatches with RuO₂ are larger: −4.7% along $[001]$ and +2.3% along $[\bar{1}10]$.

Figure 1c shows electrical resistivity $\rho(T)$ measurements for RuO₂ films, along with results for bulk RuO₂ single crystals from Ref. 15. To compare with bulk, for the thin-film samples we plot the geometric mean of the components of ρ along the two in-plane directions; the intrinsic resistive anisotropy is known to be small¹⁶, consistent with our findings (Supplementary Note 1 and Supplementary Fig. 1). $\rho(T)$ data for the lightly strained RuO₂/TiO₂(101) sample—henceforth referred to as RuO₂(101)—are nearly indistinguishable from bulk, exhibiting metallic behavior with a low residual resistivity $\rho(0.4 \text{ K}) < 2 \text{ } \mu\Omega\text{-cm}$. In contrast, a clear superconducting transition is observed for the more heavily strained RuO₂/TiO₂(110) sample—referred to as RuO₂(110)—at $T_c = 2.0 \pm 0.1 \text{ K}$.

Magnetoresistance measurements (Fig. 1e, f) with H_{\perp} applied along $[110]$ (the out-of-plane direction) show a monotonic suppression of T_c with increasing fields and an extrapolated value of $H_{cL}(T \rightarrow 0 \text{ K}) = 13.3 \pm 1.5 \text{ kOe}$, corresponding to an average in-plane superconducting coherence length of $\xi(T \rightarrow 0 \text{ K}) = 15.8 \pm 0.9 \text{ nm}$ (Supplementary Note 2 and Supplementary Fig. 2). In Fig. 1d, we show a $V(I)$ curve measured on a lithographically patterned resistivity bridge at $T/T_c = 0.3$, from which we extract a critical current density $J_c = (9.5 \pm 1.2) \times 10^4 \text{ A/cm}^2$. This large value of J_c (over one order of magnitude larger than values reported on typical elemental superconductors with comparable T_c s) indicates that the superconductivity in RuO₂(110) does not arise from a filamentary network, structural defects, minority phases, or from the substrate–film interface, which would all yield much smaller values of J_c .

In order to disentangle the effects of strain from other possible sources of superconductivity, we compare RuO₂ films as functions of strain and film thickness, t . In Fig. 2a, we plot x-ray diffraction (XRD) data from similar-thickness films of RuO₂(101) and RuO₂(110), showing that the bulk-averaged crystal structures of the films are strained as expected along the out-of-plane direction based on their net in-plane lattice mismatches with TiO₂. The primary 101 and 202 film peaks of RuO₂(101) are shifted to larger angles than bulk RuO₂, corresponding to a 1.1% compression of d_{101} , while Nelson–Riley analysis of the primary 110, 220, and 330 (see, e.g., Supplementary Fig. 4) peak positions for RuO₂(110) evidence a 2.0% expansion of d_{110} relative to bulk. In Fig. 2b, c, we plot resistivity data showing that reducing t in RuO₂(110) decreases T_c , as is commonly observed in numerous families of thin-film superconductors^{17,18}, with T_c dropping below our experimental threshold (0.4 K) between $t = 11.5$ and 5.8 nm. This suppression of T_c with thickness indicates superconductivity is not confined near the substrate–film interface, so possible interfacial modifications of the crystal structure¹⁹, carrier density²⁰, substrate–film mode coupling²¹, and non-stoichiometry in the films or substrates^{22–24} can all be eliminated as potential causes of superconductivity. These conclusions are also supported by the facts that superconductivity is not observed in RuO₂(101) films, nor in bare TiO₂ substrates treated in an identical fashion to the RuO₂ films. Finally, in Fig. 2d we include a scanning transmission electron microscopy (STEM) image of a superconducting RuO₂(110) sample, which confirms uniform growth of the film over lateral length scales exceeding those expected to be relevant for superconductivity (e.g., ξ), and shows a chemically abrupt interface between RuO₂ and TiO₂ (Supplementary Fig. 5), with no evidence of minority phases.

We believe the thickness dependence of T_c results primarily from the competition between: (i) an intrinsic strain-induced enhancement of T_c that should be maximized for thinner, commensurately strained RuO₂(110) films, versus (ii) disorder-induced suppressions of T_c that become amplified in the ultrathin limit (see, e.g., ρ_0 versus t in Fig. 2c). While the thinnest films

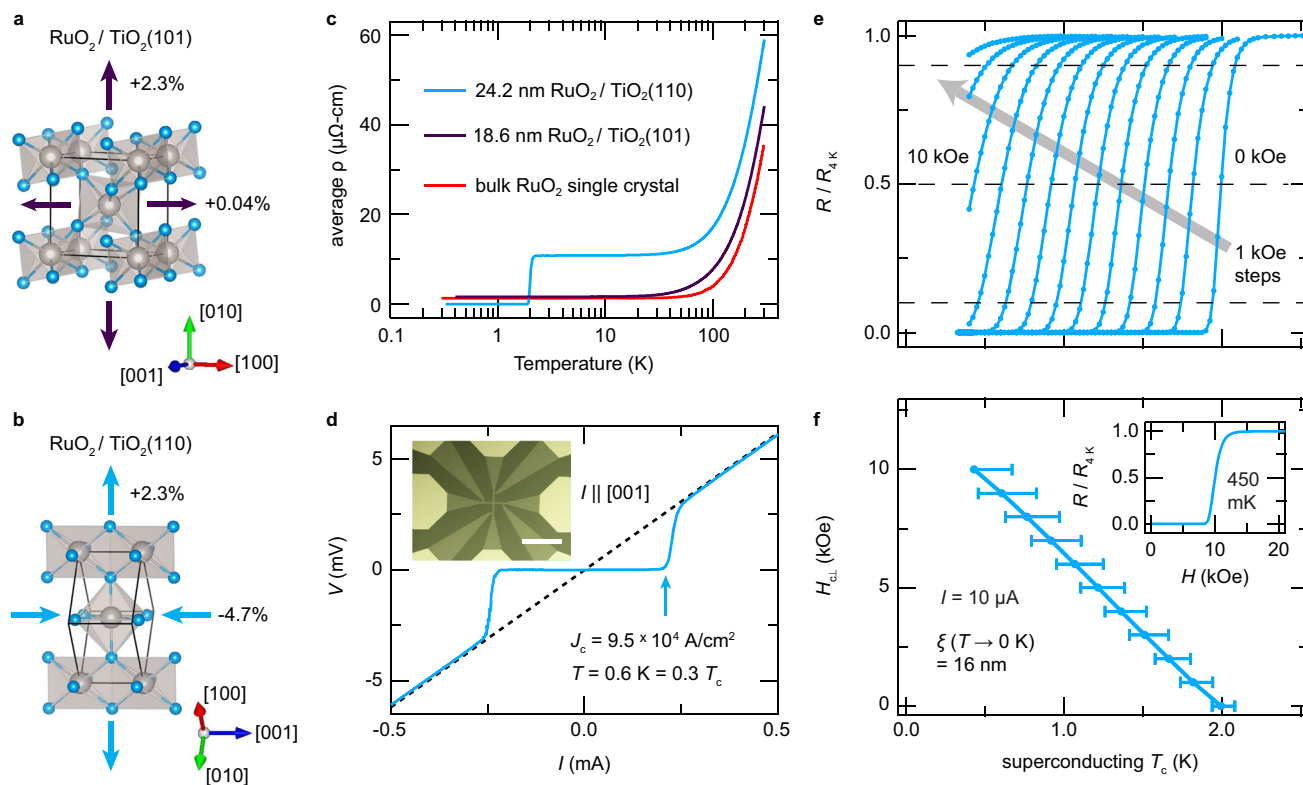


Fig. 1 Electrical transport behavior of bulk RuO_2 single crystals and epitaxially strained RuO_2 thin films. **a, b** Schematic diagrams of the crystal structures and in-plane lattice mismatches with TiO_2 substrates of RuO_2 thin films synthesized in (101)- and (110)-orientations. Gray and blue spheres represent Ru and O atoms, respectively. **c** Average resistivity versus temperature curves for 24.2 nm thick $\text{RuO}_2(110)$ and 18.6 nm thick $\text{RuO}_2(101)$ films, compared to results for bulk RuO_2 single crystals from Ref. ¹⁵. For clarity the bulk RuO_2 data have been rigidly shifted upward by $1 \mu\Omega\text{-cm}$ ($\rho_0 \approx 0.3 \mu\Omega\text{-cm}$). **d** $V(I)$ curve measured at 0.6 K on a $10 \mu\text{m}$ -wide resistivity bridge lithographically patterned on the $\text{RuO}_2(110)$ sample from (c) (as shown in the inset: scale bar = $200 \mu\text{m}$), which has the direction of current flow parallel to $[001]_{\text{rutile}}$. Similarly large critical current densities J_c are obtained with $I \parallel [1\bar{1}0]$ (Supplementary Note 1 and Supplementary Fig. 1). **e, f** Upper critical magnetic fields $H_{c\perp}$ versus superconducting T_c s extracted from magnetoresistance measurements for the $\text{RuO}_2(110)$ sample in (c) along with a characteristic $R(H)$ sweep acquired at 0.45 K (inset in (f)). Superconducting T_c s are taken as the temperatures at which the resistance crosses 50% of its residual normal-state value $R_{4\text{K}}$; error bars on these T_c s indicate where R crosses the 90% and 10% thresholds of $R_{4\text{K}}$, respectively (cf. the horizontal dashed lines in (e)).

experience the largest substrate-imposed strains, stronger disorder scattering (likely from interfacial defects) reduces T_c below our detection threshold. Films of intermediate thickness ($t \approx 10\text{--}30 \text{ nm}$) have lower residual resistivities and higher T_c s, but do exhibit signatures of partial strain relaxation. Nevertheless, a detailed analysis of misfit dislocations by STEM and XRD reciprocal-space mapping (Supplementary Notes 3, 4 and Supplementary Figs. 8–10) indicates that these films are largely structurally homogeneous and, on average, much closer to commensurately strained than fully relaxed. Finally, in much thicker samples (e.g., $t = 48 \text{ nm}$) where a more significant volume fraction of the film should be relaxed, the strain is further released by oriented micro-cracks that make such samples spatially inhomogeneous and cause severely anisotropic distributions of current flow, preventing reliable resistivity measurements (Supplementary Fig. 11).

DFT calculations and ARPES measurements. Having established the strain-induced nature of the superconductivity in $\text{RuO}_2(110)$, we now explore its underlying origin using a combination of DFT and ARPES. In Fig. 3a, we present the electronic structure of commensurately strained $\text{RuO}_2(110)$ calculated by DFT + U ($U = 2 \text{ eV}$), following the methods of Berlijn et al.¹³. Despite being constructed of RuO_6 octahedra having the same $4d^4$ electronic configuration as in $(\text{Ca,Sr,Ba})\text{RuO}_3$, the electronic structure of RuO_2 is markedly different from that of perovskite-

based ruthenates. These distinctions arise from a sizable ligand-field splitting of the t_{2g} orbitals, such that the most natural description of the low-energy electronic structure is in terms of states derived from two distinct types of orbitals: $d_{||}$ and (d_{xz}, d_{yz}) , as illustrated by plots of Wannier functions in Fig. 3b^{25,26}. Viewed in the band basis in Fig. 3a, the differentiation in \mathbf{k} -space between these orbitals becomes apparent: the near- E_F $d_{||}$ states (yellow-orange) form mostly flat bands concentrated around the $k_{001} = \pi/c$ (i.e., Z-R-A) plane, whereas the (d_{xz}, d_{yz}) states (purple) form more isotropically dispersing bands distributed uniformly throughout the Brillouin zone.

In many other d^4 ruthenates (such as Sr_2RuO_4 and Ca_2RuO_4), static mean-field electronic structure calculations (such as DFT + U) often predict quantitatively incorrect effective masses^{27–31}—and sometimes even qualitatively incorrect ground states³²—because these approaches neglect local (atomic-like) dynamical spin-orbital correlations (driven by Hund’s rules) that strongly renormalize the low-energy quasiparticle excitations. Therefore, it is imperative to compare DFT calculations for RuO_2 with experimental data, to establish the reliability of any theoretically predicted dependence of the electronic structure on strain. The left half of Fig. 3d shows the Fermi surface of $\text{RuO}_2(110)$ measured with He- 1α (21.2 eV) photons at 17 K, which agrees well with a non-magnetic DFT + U simulation of the Fermi surface at a reduced out-of-plane momentum of $k_{110} = -0.2 \pm 0.2 \pi/d_{110}$ (right half of Fig. 3d). In Fig. 3e, f, we

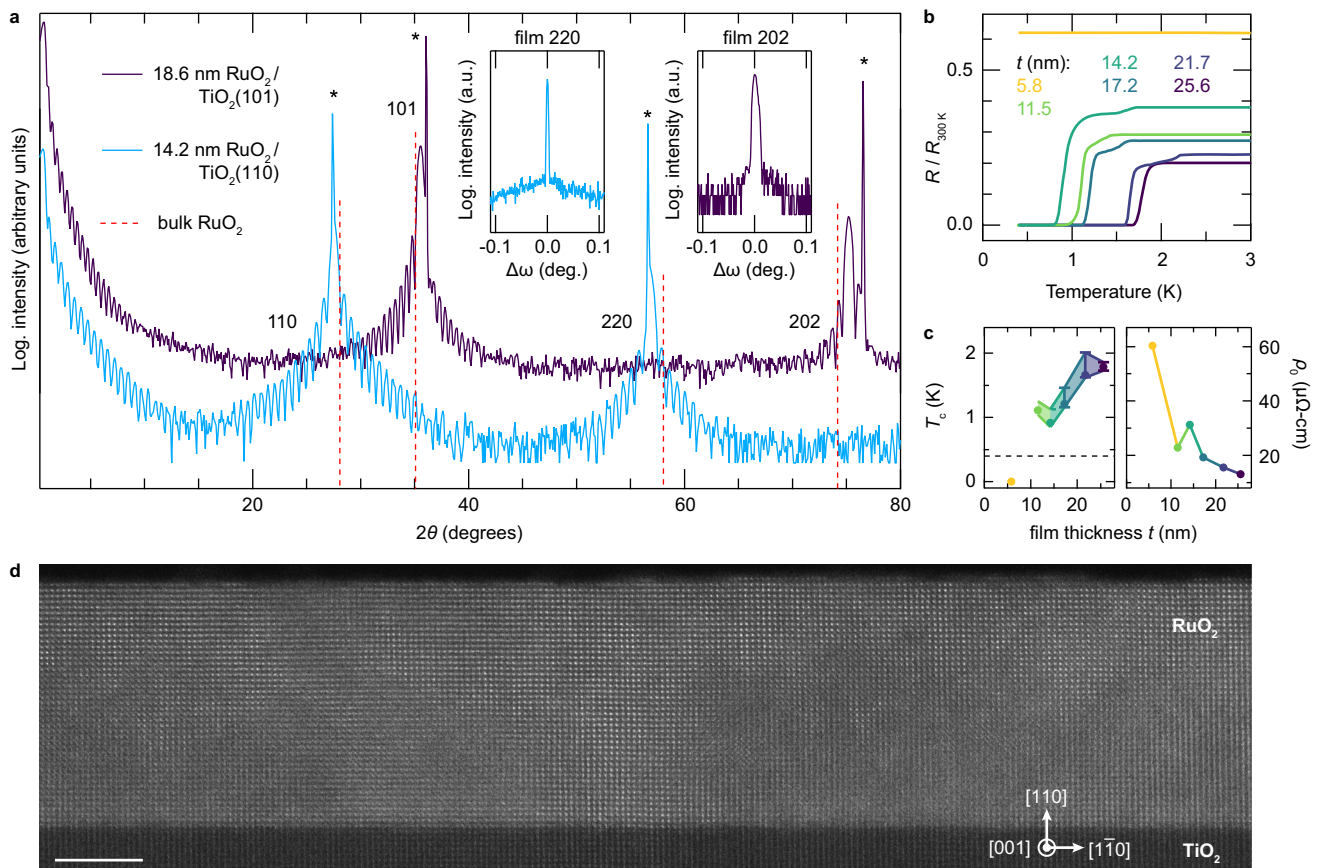


Fig. 2 Structural characterization of epitaxially strained RuO₂ thin films, and film-thickness-dependent superconductivity for RuO₂(110). **a** XRD data acquired with Cu-K α radiation along the specular crystal truncation rods for 18.6 nm thick RuO₂(101) and 14.2 nm thick RuO₂(110) films. Bragg peaks arising from the TiO₂ substrates are marked with asterisks, and the peak positions that would be expected for unstrained bulk RuO₂ are indicated by dashed red lines¹³. Insets display rocking curves with FWHMs < 0.01° acquired at the 2θ values corresponding to the primary 220 and 202 film peaks. Here q_{\parallel} is aligned with TiO₂[$\bar{1}\bar{1}0$] for the (110)-oriented sample, and with TiO₂[$\bar{1}0\bar{1}$] for the (101)-oriented sample. **b** Resistance versus temperature curves for RuO₂(110) samples with different film thicknesses t , normalized to their values at 300 K. **c** Superconducting T_c s and residual resistivities ρ_0 plotted versus film thickness for the RuO₂(110) samples from (b). Error bars on T_c s have the same meaning as in Fig. 1. The horizontal dashed line represents the base temperature attainable in our refrigerator, 0.4 K. **d** STEM image of the same 14.2 nm thick RuO₂(110) sample from (a–c) (scale bar = 5 nm). More comprehensive structural and electrical characterization of the samples shown here are included in Supplementary Notes 3, 4 and Supplementary Figs. 3–10.

plot energy versus momentum spectra acquired along the white dashed lines in Fig. 3d: in Fig. 3e, the spectrum is dominated by the flat d_{\parallel} bands centered around a binding energy of 300 meV, whereas in Fig. 3f the (d_{xz}, d_{yz}) -derived bands are steeply dispersing and can be tracked down to several hundred meV below E_F , both of which are well reproduced by DFT + U calculations. The reasonable agreement between the experimentally measured and DFT band velocities is consistent with recent ARPES studies of Ir-doped RuO₂ single crystals³³ and with earlier specific heat measurements of the Sommerfeld coefficient in bulk RuO₂, which suggested a modest momentum-averaged quasiparticle mass renormalization of $\gamma_{\text{exp.}} = 1.45\gamma_{\text{DFT}}$ ^{34,35}. The fact that the true electronic structure of RuO₂ can be well accounted for by DFT + U allows us to utilize such calculations to understand how epitaxial strains can be employed to engineer features of the electronic structure to enhance the instability towards superconductivity.

Evolution of electronic structure under strain. In Fig. 4a, we show the strain dependence of the DFT-computed band structure and DOS for RuO₂(110), RuO₂(101), and bulk RuO₂. While the results for RuO₂(101) are almost identical to bulk, the results for RuO₂(110) exhibit significant differences: the large d_{\parallel} -derived peak in the DOS (centered around a binding energy of 800 meV

for bulk) is split into multiple peaks for RuO₂(110), several of which are shifted closer to the Fermi level, thereby increasing $N(E_F)$. In our studies, we found that this strain-dependent trend was robust against details of the DFT calculations, such as whether U was finite (Supplementary Note 5 and Supplementary Fig. 12). In order to determine whether this strain dependence of $N(E_F)$ is realized in experiment, we compared the electronic structure of a thin (7 nm) highly strained RuO₂(110) film with a much thicker (48 nm) partially strain-relaxed RuO₂(110) film. The surface lattice constants of the 48 nm thick film were closer to bulk RuO₂ than the 7 nm thick film (Supplementary Note 7 and Supplementary Fig. 14), so we expect that the surface electronic structure probed by ARPES of the thicker film to be more representative of bulk RuO₂. Comparisons between the RuO₂(110) and RuO₂(101) surfaces are less straightforward, since different parts of the three-dimensional Brillouin zone are sampled by ARPES (Supplementary Note 8 and Supplementary Fig. 15). Figure 4b shows $E(k)$ spectra side by side for the 7 nm (left) and 48 nm (right) films of RuO₂(110) along the same cut through k -space from Fig. 3e where the photoemission intensity is dominated by d_{\parallel} initial states. The higher levels of strain present at the film surface for the 7 nm thick sample cause a substantial shift of the flat bands towards E_F by 120 ± 20 meV relative to the more strain-relaxed 48 nm thick sample. Integrating the

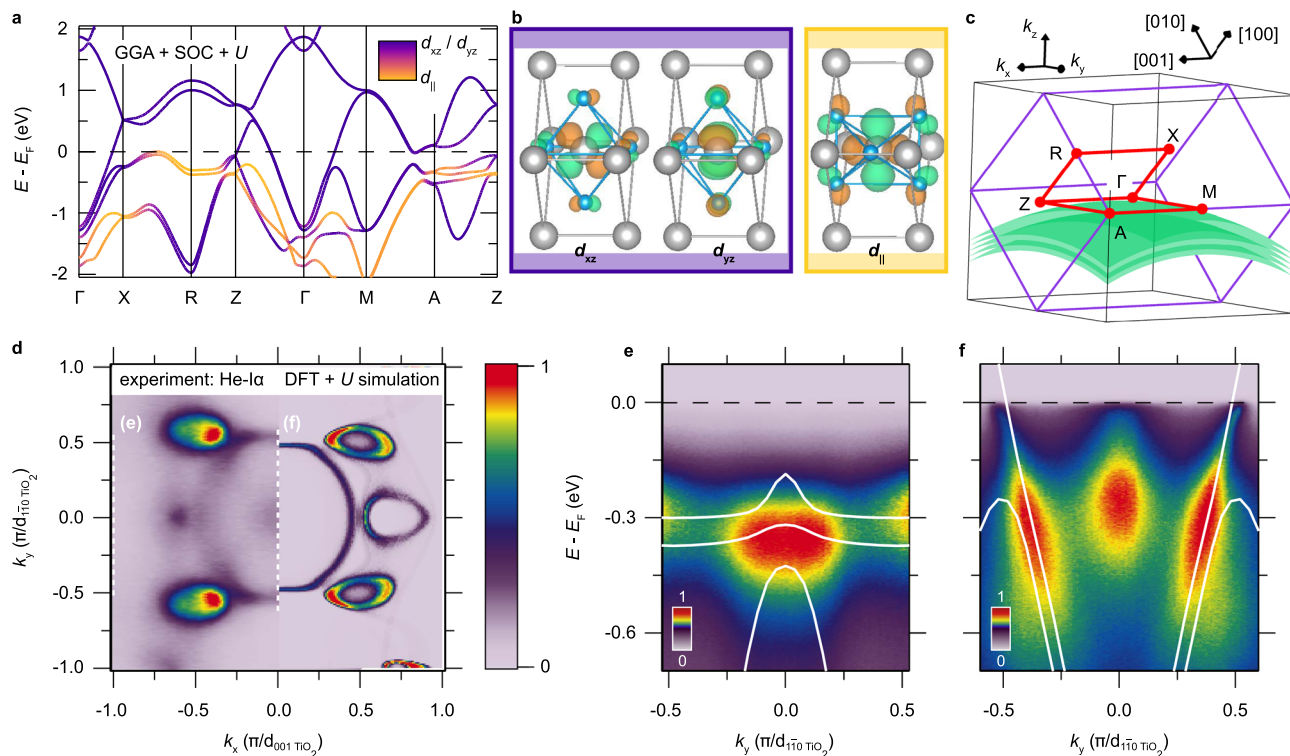


Fig. 3 Electronic structure of RuO₂. **a** Non-magnetic band structure of RuO₂(110) according to DFT, calculated within the generalized gradient approximation (GGA) including spin-orbit coupling (SOC) and a static $+U = 2$ eV correction on the Ru sites. The color scale indicates the magnitudes of projections of the Kohn-Sham eigenstates at each \mathbf{k} onto Ru-centered Wannier functions with d_{\parallel} and (d_{xz}, d_{yz}) orbital characters, which are constructed from the manifold of self-consistent eigenstates spanning E_F and are plotted in drawings of the crystal structure in **(b)**. Ru (O) atoms are colored gray (blue), as in Fig. 1a, b. Green and orange surfaces in **(b)** represent isosurfaces of the Wannier functions that have equal absolute magnitudes, but opposite (i.e., positive and negative) signs, respectively. **c** Brillouin zone schematic defining the coordinate system utilized for describing ARPES measurements of the electronic structure on (110)-oriented surfaces: $k_x \parallel [001]_{\text{rutile}}$, $k_y \parallel [\bar{1}\bar{1}0]_{\text{rutile}}$, and $k_z \parallel [110]_{\text{rutile}}$. The Brillouin zone of the parent tetragonal rutile structure is outlined in purple, the high-symmetry contour for the spaghetti plot from **(a)** is colored red, and the region probed on (110)-oriented surfaces with He-I α photons (21.2 eV) is shaded green (Supplementary Note 6 and Supplementary Fig. 13). **d** Slice through the Fermi surface experimentally measured for a 7 nm thick RuO₂(110) film (left), compared to the Fermi surface from DFT + U simulations (right) projected onto the region of the Brillouin zone colored green in **(c)**. $E(k)$ spectra acquired along the one-dimensional cuts indicated by dashed white lines in **(d)** show: **e** flat bands with d_{\parallel} orbital character and **f** more dispersive bands with (d_{xz}, d_{yz}) character, both consistent with DFT + U expectations (solid white lines). The intensities of the experimental data shown in **(d-f)** and of the DFT simulations shown in **(d)** are plotted in arbitrary units where we define 0 (1) to be the minimum (maximum) value, respectively, of the given data set. Only relative changes in intensity within a given panel (as visualized by the false color scales) are meaningful.

ARPES data over the full measured region of \mathbf{k} -space for both samples gives the average energy distribution curves plotted in Fig. 4c, which show that spectral weight near E_F is enhanced as the d_{\parallel} states move towards E_F , in qualitative agreement with the trend predicted by DFT. Our results indicate that the primary electronic effect of the epitaxial strains in RuO₂(110) is to alter the relative occupancies of the d_{\parallel} and (d_{xz}, d_{yz}) orbitals as compared with bulk, and to push a large number of states with d_{\parallel} character closer to E_F , which enhances $N(E_F)$ and likely T_c .

Discussion

Observations of Fermi-liquid-like quasiparticles near E_F ^{34,36–38} that scatter at higher energies primarily via their interaction with phonons^{16,35}, along with the fact that superconductivity in RuO₂(110) persists in the dirty limit (Supplementary Note 4 and Supplementary Fig. 9), are both consistent with conventional Cooper pairing, suggesting that calculations assuming an electron-phonon mechanism may be enlightening. We performed DFT-based Migdal-Eliashberg calculations of T_c for bulk RuO₂ and commensurately strained RuO₂(110) that indeed indicate epitaxial strain can enhance T_c by several orders of magnitude. For bulk RuO₂, we find that the empirical Coulomb

pseudopotential must satisfy $\mu^* > 0.30$ to be compatible with the experimentally measured least upper bound on T_c ($T_c < 0.3$ K¹⁵). For this range of μ^* , T_c for RuO₂(110) can be as high as 7 K (Supplementary Note 9 and Supplementary Fig. 16). A robust strain-induced enhancement of the electron-phonon coupling $\lambda_{\text{el-ph}}$ boosts T_c by a factor of 20 (for $\mu^* = 0.30$), and this ratio becomes even larger for higher values of μ^* —e.g., for $\mu^* = 0.37$, $T_c(110)/T_c(\text{bulk}) = 5$ K/5 mK). Although these estimations of T_c are broadly consistent with our experimental findings, conventional superconductivity in RuO₂ remains a working hypothesis until measurements of the order parameter are possible.

In principle, assuming that all Fermi liquids are eventually unstable towards some channel(s) of Cooper pairing at sufficiently low temperatures and magnetic fields (including internal fields arising from magnetic impurities), the strain-stabilized superconductivity observed here in RuO₂ is not strictly a change in the ground state of the system. For our purposes, however, extremely low temperatures and fields below what are experimentally achievable can be regarded as effectively zero, justifying our use of phrases such as strain-induced superconductivity interchangeably with huge enhancement of critical temperature. If we limit the scope of this semantic discussion to conventional,

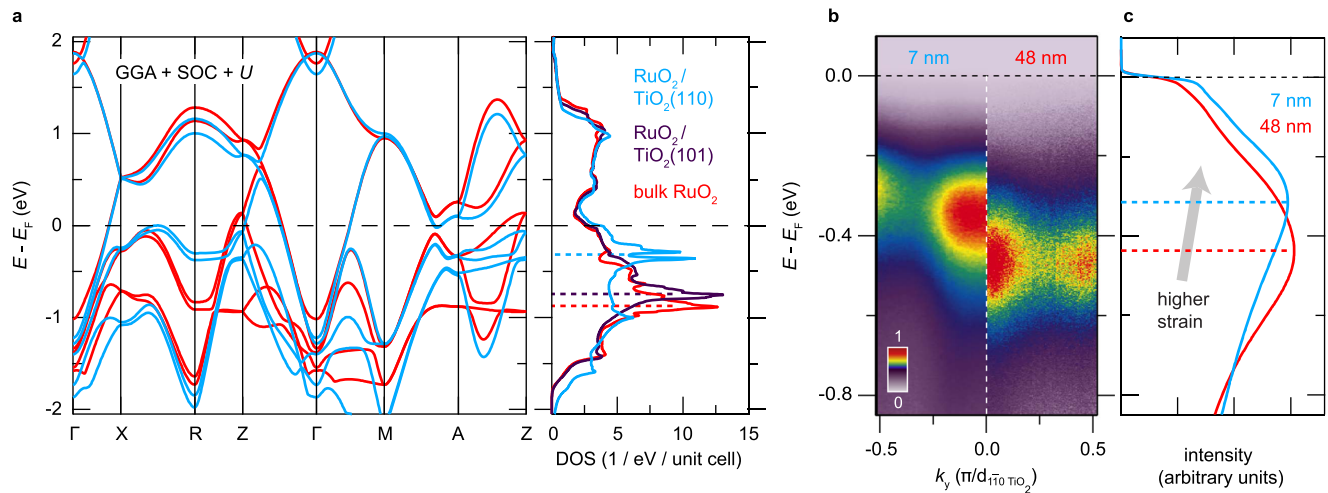


Fig. 4 Strain-induced changes to the electronic structure of RuO₂. **a** DFT + *U* (*U* = 2 eV) band structures and corresponding density of states (DOS) traces for bulk RuO₂ and epitaxially strained RuO₂(110) and RuO₂(101) thin films. The RuO₂(101) results are omitted from the spaghetti plot for clarity since they are very similar to bulk. **b** Comparison of *E*(*k*) spectra along the cut shown in Fig. 3e for two different RuO₂(110) samples: a highly strained 7 nm thick film (left), and a partially strain-relaxed 48 nm thick film (right). The false color scale used to visualize the intensities in each spectrum is defined and normalized in the same way as in Fig. 3. **c** As an approximate proxy of the total DOS, for these samples we plot the energy distribution curves of photoemission intensity averaged over the entire region of *k*-space probed experimentally with 21.2 eV photons (cf. Fig. 3c), which demonstrate that the epitaxial strains imposed by TiO₂(110) substrates shift *d*_{||} states towards *E*_{*F*} and thereby increase *N*(*E*_{*F*}).

non-sign-changing (*s*-wave) order parameters, we note that in the presence of Coulomb repulsion and other effects, an instability towards *s*-wave superconductivity is not present in every system; the electron–phonon coupling generally must exceed some finite critical value. In the present context, the effects of strain reported in this article might be boosting the electron–phonon coupling above the critical value appropriate for RuO₂, thus inducing a new *s*-wave state that is absent (even in theory) for the unstrained material.

We believe our results demonstrate that a promising strategy to create new transition-metal superconductors is to apply judiciously chosen anisotropic strains that modulate degeneracies among *d* orbitals near *E*_{*F*}. Many classic studies of conventional superconductors that have nearly-free-electron states spanning *E*_{*F*} derived from (*s*, *p*) orbitals actually show decreases in *T*_{*c*} under hydrostatic pressure³⁹, due to lattice stiffening dominating over any pressure-induced changes to the Hopfield parameter⁴⁰. In a limited number of elemental metals where *T*_{*c*} monotonically increases under pressure (such as vanadium⁴¹), pressure-induced electron transfer between *s* → *d* orbitals has been suggested as a likely cause of the enhanced transition temperatures³; a drawback of this approach, however, is that large pressures of ≈ 10 GPa are typically required to, e.g., double *T*_{*c*}. More recently, measurements on single crystals of the unconventional superconductor Sr₂RuO₄ have shown that appropriately oriented uniaxial pressures of only ≈ 1 GPa can boost *T*_{*c*} by more than a factor of two⁴². Independent of the underlying mechanism, it appears that anisotropic strains may prove to be significantly more efficacious than hydrostatic pressure for tuning superconductivity in multi-orbital systems, as shown here for RuO₂, as well as in Sr₂RuO₄.

Sizable coupling between the lattice and electronic degrees of freedom in rutile-like crystal structures has been well established both theoretically²⁶ and experimentally in VO₂, where strain-induced variations in the orbital occupancies can be used to modify the metal–insulator transition temperature by $\delta T_{\text{MIT}} \approx 70$ K^{43,44}. Therefore, it may be promising to explore other less strongly correlated (i.e., 4*d* and 5*d*) rutile compounds such as MoO₂ for strain-stabilized superconductivity, instead of employing chemical doping^{45–47}. Finally, since RuO₂/TiO₂(110)

is the first known stoichiometric superconductor within the rutile family, further optimization of the superconductivity may enable the creation of structures that integrate superconductivity with other functional properties that have been extensively studied in other rutile compounds, such as high photocatalytic efficiency, half-metallic ferromagnetism, and large spin Hall conductivities.

Methods

Film synthesis. Epitaxial thin films of RuO₂ were synthesized on various orientations of rutile TiO₂ substrates using a GEN10 reactive oxide MBE system (Veeco Instruments). Prior to growth, TiO₂ substrates (Crystec, GmbH) were cleaned with organic solvents, etched in acid, and annealed in air to produce starting surfaces with step-terrace morphology, following the methods in Ref. 48. Elemental ruthenium (99.99% purity, ESPI Metals) was evaporated using an electron-beam evaporator in background oxidant partial pressures of $1 \times 10^{-6} - 5 \times 10^{-6}$ Torr of distilled ozone (≈ 80% O₃ + 20% O₂) at substrate temperatures of 250–400 °C, as measured by a thermocouple. Reflection high-energy electron diffraction was used to monitor the surface crystallinity of the films in situ and showed characteristic oscillations in intensity during most of the Ru deposition, indicating a layer-by-layer growth mode following the initial nucleation of several-monolayer-thick RuO₂ islands⁴⁹.

Film characterization. The crystal structures of all RuO₂ thin-film samples were characterized via lab-based x-ray diffraction (XRD) measurements with Cu-*K* α radiation (Rigaku SmartLab and Malvern Panalytical Empyrean diffractometers). Four-point-probe electrical transport measurements were conducted from 300 K down to a base temperature of 0.4 K using a Physical Properties Measurement System equipped with a He-3 refrigerator (Quantum Design). All RuO₂/TiO₂(110) samples were superconducting with *T*_{*c*}s ranging from 0.5 to 2.4 K, except for ultrathin films with residual resistivities $\rho_0 \approx 40 \mu\Omega\text{-cm}$, as shown in Fig. 2 and Supplementary Fig. 9.

A subset of films studied by XRD and transport were also characterized in situ by ARPES and low-energy electron diffraction (LEED). For these measurements, films were transferred under ultrahigh vacuum immediately following growth to an analysis chamber with a base pressure of 5×10^{-11} Torr equipped with a helium plasma discharge lamp, a hemispherical electron analyzer (VG Scienta R4000), and a four-grid LEED optics (SPECS ErLEED 150).

A subset of films studied by XRD and transport were also imaged using cross-sectional STEM. Cross-sectional specimens were prepared using the standard focused ion beam (FIB) lift-out process on a Thermo Scientific Helios G4 X FIB. High-angle annular dark-field STEM (HAADF-STEM) images were acquired on an aberration-corrected FEI Titan Themis at 300 keV with a probe convergence semi-angle of 21.4 mrad and inner and outer collection angles of 68 and 340 mrad.

Electronic structure calculations. Non-magnetic DFT calculations for the electronic structure of RuO₂ were performed using the Quantum ESPRESSO software

package^{50,51} with fully relativistic ultrasoft pseudopotentials for Ru and O⁵². We represented the Kohn-Sham wavefunctions in a basis set of plane waves extending up to a kinetic energy cutoff of 60 Ry, and used a cutoff of 400 Ry for representing the charge density. Brillouin zone integrations were carried out on an $8 \times 8 \times 12$ k -mesh with 70 meV of Gaussian smearing. Perdew, Burke, and Ernzerhof's parametrization of the generalized gradient approximation was employed as the exchange-correlation functional⁵³, supplemented by an on-site correction of $+U_{\text{eff}} = U - J = 2$ eV within spheres surrounding the Ru sites, following Ref. 13.

After obtaining self-consistent Kohn-Sham eigenstates via DFT, we used the pw2wannier and Wannier90 codes⁵⁴ to construct 20 Wannier functions spanning the manifold of eigenstates surrounding E_F (20 = 10 d -orbitals per Ru atom \times 2 Ru atoms per unit cell). Following Ref. 55, to account for the non-symmorphic space group symmetries of rutile crystal structures, we referenced the trial orbitals employed in the Wannierisation routine to locally rotated coordinate systems centered on the two Ru sites within each unit cell. Orbital designations employed in the main text such as $d_{||}$ and (d_{xz}, d_{yz}) refer to projections onto this basis of Wannier functions. The more computationally efficient Wannier basis was used to calculate quantities that required dense k meshes to be properly converged, such as the projected Fermi surface in Fig. 3d ($51 \times 51 \times 51$ k -mesh) and the near- E_F density of states traces in Fig. 4a ($32 \times 32 \times 48$ k -meshes).

Because the RuO₂ samples studied in this work are thin films subject to biaxial epitaxial strains imposed by differently oriented rutile TiO₂ substrates, we performed DFT + Wannier calculations of the electronic structure for several different crystal structures of RuO₂ as described in Supplementary Note 5 and Supplementary Table 1. We used the ISOTROPY software package⁵⁶ to study distortions of the parent tetragonal rutile crystal structure that are induced in biaxially strained thin films. Crystal structures and Wannier functions were visualized using the VESTA software package⁵⁷.

Electron-phonon coupling calculations. To generate the inputs required for the electron-phonon coupling calculations described below, first-principles electronic structure and phonon calculations were performed using the Quantum ESPRESSO software package with norm-conserving pseudopotentials and plane-wave basis sets^{50,51}. Here we employed a kinetic energy cutoff of 160 Ry, an electronic momentum k -point mesh of $16 \times 16 \times 24$, 20 meV of Methfessel-Paxton smearing for the occupation of the electronic states, and a tolerance of 10^{-10} eV for the total energy convergence. The generalized gradient approximation as implemented in the PBEsol functional⁵⁸ was employed as the exchange-correlation functional. For the Wannier interpolation, we used an interpolating electron-momentum mesh of $8 \times 8 \times 12$ and a phonon-momentum mesh of $2 \times 2 \times 3$. Results for bulk RuO₂ were calculated using the crystal structure that minimizes the DFT-computed total energy with the PBEsol functional: ($a = 4.464$ Å, $c = 3.093$ Å) and $x_{\text{oxygen}} = 0.3062$. Results for strained RuO₂(110) were calculated by changing the lattice constants of this simulated bulk crystal structure by +2.3% along [110], -4.7% along [001], +2.2% along [110], and setting $x_{\text{oxygen}} = y_{\text{oxygen}} = 0.2996$. The lattice parameter along [110] and internal coordinates of this simulated RuO₂(110) structure were determined by allowing the structure to relax so as to (locally) minimize the DFT-computed total energy.

Electron-phonon coupling calculations were performed using the EPW code⁵⁹, using an interpolated electron-momentum mesh of $32 \times 32 \times 48$ and an interpolated phonon-momentum mesh of $8 \times 8 \times 12$. The isotropic Eliashberg spectral function $\alpha^2F(\omega)$ and total electron-phonon coupling constant $\lambda_{\text{el-ph}}$ (integrated over all phonon modes and wavevectors) were calculated with a phonon smearing of 0.2 meV. From the calculated $\alpha^2F(\omega)$ and $\lambda_{\text{el-ph}}$, we estimated the superconducting transition temperature using the semi-empirical McMillan-Allen-Dynes formula^{60,61}:

$$T_c = \frac{\omega_{\text{log}}}{1.2} \exp \left[-\frac{1.04(1 + \lambda_{\text{el-ph}})}{\lambda_{\text{el-ph}} - \mu^*(1 + 0.62\lambda_{\text{el-ph}})} \right] \quad (2)$$

Data availability

The data supporting the findings of this study are available within the paper and supplementary information. Data connected to the study from PARADIM facilities are available at paradim.org. Any additional data connected to the study are available from the corresponding author upon reasonable request.

Received: 19 August 2020; Accepted: 19 November 2020;

Published online: 04 January 2021

References

- Carbotte, J. P. Properties of boson-exchange superconductors. *Rev. Mod. Phys.* **62**, 1027–1157 (1990).
- Morel, P. & Anderson, P. W. Calculation of the superconducting state parameters with retarded electron-phonon interaction. *Phys. Rev.* **125**, 1263–1271 (1962).
- Hamlin, J. J. Superconductivity in the metallic elements at high pressures. *Phys. C* **514**, 59–76 (2015).
- Burganov, B. et al. Strain control of fermiology and many-body interactions in two-dimensional ruthenates. *Phys. Rev. Lett.* **116**, 197003 (2016).
- Ohtomo, A. & Hwang, H. Y. A high-mobility electron gas at the LaAlO₃/SrTiO₃ heterointerface. *Nature* **427**, 423 (2004).
- Kawasaki, J. K. et al. Rutile IrO₂/TiO₂ superlattices: a hyperconnected analog to the Ruddeldsen-Popper structure. *Phys. Rev. Mater.* **2**, 054206 (2018).
- Lock, J. M. & Bragg, W. L. Penetration of magnetic fields into superconductors III. Measurements on thin films of tin, lead and indium. *Proc. R. Soc. Lond. Ser. A* **208**, 391–408 (1951).
- Locquet, J.-P. et al. Doubling the critical temperature of La_{1.9}Sr_{0.1}CuO₄ using epitaxial strain. *Nature* **394**, 453 (1998).
- Si, W., Li, H.-C. & Xi, X. X. Strain and oxygenation effects on superconductivity of La_{1.85}Sr_{0.15}CuO₄ thin films. *Appl. Phys. Lett.* **74**, 2839–2841 (1999).
- Si, W. & Xi, X. X. Epitaxial-strain-induced insulator-superconductor transition in undoped and lightly doped La₂CuO₄. *Appl. Phys. Lett.* **78**, 240–242 (2001).
- Bozovic, I., Logvenov, G., Belca, I., Narimbetov, B. & Sveklo, I. Epitaxial strain and superconductivity in La_{2-x}Sr_xCuO₄ thin films. *Phys. Rev. Lett.* **89**, 107001 (2002).
- Engelmann, J. et al. Strain induced superconductivity in the parent compound BaFe₂As₂. *Nat. Commun.* **4**, 2877 (2013).
- Berlijn, T. et al. Itinerant antiferromagnetism in RuO₂. *Phys. Rev. Lett.* **118**, 077201 (2017).
- Burdett, J. K., Hughbanks, T., Miller, G. J., Richardson, J. W. & Smith, J. V. Structural-electronic relationships in inorganic solids: powder neutron diffraction studies of the rutile and anatase polymorphs of titanium dioxide at 15 and 295 K. *J. Am. Chem. Soc.* **109**, 3639–3646 (1987).
- Lin, J. J. et al. Low temperature electrical transport properties of RuO₂ and IrO₂ single crystals. *J. Phys.: Condens. Matter* **16**, 8035 (2004).
- Ryden, W. D., Lawson, A. W. & Sartain, C. C. Electrical transport properties of IrO₂ and RuO₂. *Phys. Rev. B* **1**, 1494–1500 (1970).
- Pinto, N. et al. Dimensional crossover and incipient quantum size effects in superconducting niobium nanofilms. *Sci. Rep.* **8**, 4710 (2018).
- Meyer, T. L., Jiang, L., Park, S., Egami, T. & Lee, H. N. Strain-relaxation and critical thickness of epitaxial La_{1.85}Sr_{0.15}CuO₄ films. *APL Mater.* **3**, 126102 (2015).
- Gozar, A. et al. High-temperature interface superconductivity between metallic and insulating copper oxides. *Nature* **455**, 782–785 (2008).
- He, S. et al. Phase diagram and electronic indication of high-temperature superconductivity at 65 K in single-layer FeSe films. *Nat. Mater.* **12**, 605–610 (2013).
- Lee, J. J. et al. Interfacial mode coupling as the origin of the enhancement of T_c in FeSe films on SrTiO₃. *Nature* **515**, 245–248 (2014).
- Paik, H. et al. Transport properties of ultra-thin VO₂ films on (001) TiO₂ grown by reactive molecular-beam epitaxy. *Appl. Phys. Lett.* **107**, 163101 (2015).
- Quackenbush, N. F. et al. Reducing orbital occupancy in VO₂ suppresses Mott physics while Peierls distortions persist. *Phys. Rev. B* **96**, 081103 (2017).
- Yoshimatsu, K., Sakata, O. & Ohtomo, A. Superconductivity in Ti₄O₇ and γ -Ti₃O₅ films. *Sci. Rep.* **7**, 12544 (2017).
- Goodenough, J. B. The two components of the crystallographic transition in VO₂. *J. Solid State Chem.* **3**, 490–500 (1971).
- Eyert, V., Horny, R., Hoeck, K.-H. & Horn, S. Embedded Peierls instability and the electronic structure of MoO₂. *J. Phys.: Condens. Matter* **12**, 4923 (2000).
- Mackenzie, A. P. et al. Quantum oscillations in the layered perovskite superconductor Sr₂RuO₄. *Phys. Rev. Lett.* **76**, 3786–3789 (1996).
- Mravlje, J. et al. Coherence-incoherence crossover and the mass-renormalization puzzles in Sr₂RuO₄. *Phys. Rev. Lett.* **106**, 096401 (2011).
- Tamai, A. et al. High-resolution photoemission on Sr₂RuO₄ reveals correlation-enhanced effective spin-orbit coupling and dominantly local self-energies. *Phys. Rev. X* **9**, 021048 (2019).
- Ricco, S. et al. In situ strain tuning of the metal-insulator-transition of Ca₂RuO₄ in angle-resolved photoemission experiments. *Nat. Commun.* **9**, 4535 (2018).
- Sutter, D. et al. Orbital selective breakdown of Fermi liquid quasiparticles in Ca_{1.8}Sr_{0.2}RuO₄. *Phys. Rev. B* **99**, 121115 (2019).
- Sutter, D. et al. Hallmarks of Hund's coupling in the Mott insulator Ca₂RuO₄. *Nat. Commun.* **8**, 15176 (2017).
- Jovic, V. et al. Dirac nodal lines and flat-band surface state in the functional oxide RuO₂. *Phys. Rev. B* **98**, 241101 (2018).
- Passenheim, B. C. & McCollum, D. C. Heat capacity of RuO₂ and IrO₂ between 0.54 and 10 K. *J. Chem. Phys.* **51**, 320–321 (1969).
- Glassford, K. M. & Chelikowsky, J. R. Electron transport properties in RuO₂ rutile. *Phys. Rev. B* **49**, 7107–7114 (1994).

36. Marcus, S. M. & Butler, S. R. Measurement of the de Haas-van Alphen effect in the rutile structure RuO₂. *Phys. Lett. A* **26**, 518–519 (1968).
37. Slivka, R. T. & Langenberg, D. N. Azbel-Kaner cyclotron resonance in ruthenium dioxide. *Phys. Lett. A* **28**, 169–170 (1968).
38. Graebner, J. E., Greiner, E. S. & Ryden, W. D. Magnetothermal oscillations in RuO₂, OsO₂, and IrO₂. *Phys. Rev. B* **13**, 2426–2432 (1976).
39. Smith, T. F. & Chu, C. W. Will pressure destroy superconductivity? *Phys. Rev.* **159**, 353–358 (1967).
40. Hopfield, J. J. Angular momentum and transition-metal superconductivity. *Phys. Rev.* **186**, 443–451 (1969).
41. Ishizuka, M., Iketani, M. & Endo, S. Pressure effect on superconductivity of vanadium at megabar pressures. *Phys. Rev. B* **61**, R3823–R3825 (2000).
42. Steppke, A. et al. Strong peak in T_c of Sr₂RuO₄ under uniaxial pressure. *Science* **355**, eaaf9398 (2017).
43. Muraoka, Y. & Hiroi, Z. Metal-insulator transition of VO₂ thin films grown on TiO₂ (001) and (110) substrates. *Appl. Phys. Lett.* **80**, 583–585 (2002).
44. Aetukuri, N. B. et al. Control of the metal-insulator transition in vanadium dioxide by modifying orbital occupancy. *Nat. Phys.* **9**, 661–666 (2013).
45. Alves, L. M. S. et al. Unconventional metallic behavior and superconductivity in the K-Mo-O system. *Phys. Rev. B* **81**, 174532 (2010).
46. Alves, L. M. S. et al. Superconductivity and magnetism in the K_xMoO_{2-δ}. *J. Appl. Phys.* **112**, 073923 (2012).
47. Parker, D., Idrobo, J. C., Cantoni, C. & Sefat, A. S. Evidence for superconductivity at $T_c = 12$ K in oxygen-deficient MoO_{2-δ} and properties of molybdenum arsenide and oxide binaries. *Phys. Rev. B* **90**, 054505 (2014).
48. Yamamoto, Y., Nakajima, K., Ohsawa, T., Matsumoto, Y. & Koinuma, H. Preparation of atomically smooth TiO₂ single crystal surfaces and their photochemical property. *Jpn. J. Appl. Phys.* **44**, L511 (2005).
49. He, Y., Langsdorf, D., Li, L. & Over, H. Versatile model system for studying processes ranging from heterogeneous to photocatalysis: epitaxial RuO₂(110) on TiO₂(110). *J. Phys. Chem. C* **119**, 2692–2702 (2015).
50. Giannozzi, P. et al. QUANTUM ESPRESSO: a modular and open-source software project for quantum simulations of materials. *J. Phys.: Condens. Matter* **21**, 395502 (2009).
51. Giannozzi, P. et al. Advanced capabilities for materials modelling with Quantum ESPRESSO. *J. Phys.: Condens. Matter* **29**, 465901 (2017).
52. Dal Corso, A. Pseudopotentials periodic table: from H to Pu. *Comp. Mater. Sci.* **95**, 337–350 (2014).
53. Perdew, J. P., Burke, K. & Ernzerhof, M. Generalized gradient approximation made simple. *Phys. Rev. Lett.* **77**, 3865–3868 (1996).
54. Mostofi, A. A. et al. An updated version of wannier90: a tool for obtaining maximally-localised Wannier functions. *Comput. Phys. Commun.* **185**, 2309–2310 (2014).
55. Eyert, V. The metal-insulator transitions of VO₂: a band theoretical approach. *Ann. der Phys.* **11**, 650–704 (2002).
56. Stokes, H. T., Hatch, D. M. & Campbell, B. J. ISOTROPY Software Suite. [iso.byu.edu](http://www.byu.edu).
57. Momma, K. & Izumi, F. VESTA 3 for three-dimensional visualization of crystal, volumetric and morphology data. *J. Appl. Crystallogr.* **44**, 1272–1276 (2011).
58. Perdew, J. P. et al. Restoring the density-gradient expansion for exchange in solids and surfaces. *Phys. Rev. Lett.* **100**, 136406 (2008).
59. Ponce, S., Margine, E. R., Verdi, C. & Giustino, F. EPW: electron-phonon coupling, transport and superconducting properties using maximally localized Wannier functions. *Comput. Phys. Commun.* **209**, 116–133 (2016).
60. McMillan, W. L. Transition temperature of strong-coupled superconductors. *Phys. Rev.* **167**, 331–344 (1968).
61. Allen, P. B. & Dynes, R. C. Transition temperature of strong-coupled superconductors reanalyzed. *Phys. Rev. B* **12**, 905–922 (1975).

Acknowledgements

The authors thank Y. Li for assistance with electrical transport measurements. This work was supported through the National Science Foundation (Platform for the Accelerated Realization, Analysis, and Discovery of Interface Materials, PARADIM) under Cooperative Agreement No. DMR-1539918, NSF DMR-1709255, the Air Force Office of Scientific Research Grant No. FA9550-15-1-0474, and the Department of Energy (Award No. DE-SC0019414). This research was funded in part by the Gordon and Betty Moore Foundation's EPiQS Initiative through Grant Nos. GBMF3850 and GBMF9073 to Cornell University. This work made use of the Cornell Center for Materials Research (CCMR) Shared Facilities, which are supported through the NSF MRSEC Program (No. DMR-1719875). The FEI Titan Themis 300 was acquired through NSF-MRI-1429155, with additional support from Cornell University, the Weill Institute, and the Kavli Institute at Cornell. Device fabrication and substrate preparation were performed in part at the Cornell NanoScale Facility, a member of the National Nanotechnology Coordinated Infrastructure (NNCI), which is supported by the NSF (Grant No. ECCS-1542081).

Author contributions

H.P., N.J.S., and H.P.N. synthesized the samples by MBE. J.P.R., H.P., N.J.S., and H.P.N. characterized the samples by XRD. J.P.R., L.M., and Y.L. characterized the samples by electrical transport; L.M. lithographically patterned resistivity bridges on select films. J.P.R., J.K.K., J.N.N., and B.D.F. characterized the samples by ARPES and LEED. B.H.G. characterized the samples by STEM, J.P.R. performed DFT calculations of the electronic structure, and B.P. performed DFT-based calculations of the electron-phonon coupling. L.F.K., D.G.S., and K.M.S. supervised the various aspects of this project. J.P.R. and K.M.S. wrote the manuscript with input from all authors.

Competing interests

The authors declare no competing interests.

Additional information

Supplementary information is available for this paper at <https://doi.org/10.1038/s41467-020-20252-7>.

Correspondence and requests for materials should be addressed to J.P.R. or K.M.S.

Peer review information *Nature Communications* thanks the anonymous reviewers for their contribution to the peer review of this work.

Reprints and permission information is available at <http://www.nature.com/reprints>

Publisher's note Springer Nature remains neutral with regard to jurisdictional claims in published maps and institutional affiliations.



Open Access This article is licensed under a Creative Commons Attribution 4.0 International License, which permits use, sharing, adaptation, distribution and reproduction in any medium or format, as long as you give appropriate credit to the original author(s) and the source, provide a link to the Creative Commons license, and indicate if changes were made. The images or other third party material in this article are included in the article's Creative Commons license, unless indicated otherwise in a credit line to the material. If material is not included in the article's Creative Commons license and your intended use is not permitted by statutory regulation or exceeds the permitted use, you will need to obtain permission directly from the copyright holder. To view a copy of this license, visit <http://creativecommons.org/licenses/by/4.0/>.

© The Author(s) 2021

Supplementary Information: Strain-stabilized superconductivity

J. P. Ruf,¹ H. Paik,² N. J. Schreiber,³ H. P. Nair,³ L. Miao,¹ J. K. Kawasaki,^{1,4} J. N. Nelson,¹ B. D. Faeth,¹ Y. Lee,¹ B. H. Goodge,^{5,6} B. Pamuk,⁵ C. J. Fennie,⁵ L. F. Kourkoutis,^{5,6} D. G. Schlom,^{3,6} and K. M. Shen^{1,6}

¹*Department of Physics, Laboratory of Atomic and Solid State Physics, Cornell University, Ithaca, NY 14853, USA*

²*Platform for the Accelerated Realization, Analysis, and Discovery of Interface Materials (PARADIM), Cornell University, Ithaca, New York 14853, USA*

³*Department of Materials Science and Engineering, Cornell University, Ithaca, NY 14853, USA*

⁴*Department of Materials Science and Engineering, University of Wisconsin, Madison WI 53706*

⁵*School of Applied and Engineering Physics, Cornell University, Ithaca, New York 14853, USA*

⁶*Kavli Institute at Cornell for Nanoscale Science, Ithaca, NY 14853, USA*

Supplementary Note 1: ELECTRICAL TRANSPORT MEASUREMENTS ON PATTERNED RESISTIVITY BRIDGES

In Supplementary Fig. 1, we show how the electrical transport properties of an RuO₂/TiO₂(110) sample depend on the direction of current flow in the film when it is confined to flow along the orthogonal in-plane crystallographic axes, [001] and [1 $\bar{1}$ 0]. Prior to lithographically patterning resistivity bridges on the film, we measured the resistance versus temperature of the entire 10 mm \times 10 mm \times 24.2 nm thick film by wire bonding four contacts directly to the surface of the sample in an in-line contact geometry. Such a contact geometry probes the geometric mean of the two diagonal components of the in-plane resistivity tensor, i.e. $\sqrt{\rho_{001}\rho_{1\bar{1}0}}$, neglecting small finite-size corrections that depend on how the contacts are oriented relative to the edges of the wafer [1]. The results of these measurements are shown by the blue traces in Supplementary Fig. 1a-b; these are the same data plotted on a logarithmic temperature scale in Fig. 1c of the main text.

Since RuO₂ has a tetragonal crystal structure in bulk (and orthorhombic or perhaps monoclinic in (110)-oriented films), ρ_{001} and $\rho_{1\bar{1}0}$ are not guaranteed by symmetry to be equal. The intrinsic transport anisotropy in bulk RuO₂ is known to be small, with differences between ρ_{100} and ρ_{001} that are less than 10% at 300 K [2, 3]; however, in heteroepitaxial thin films it is common for highly oriented structural defects—e.g., those nucleated at step edges on the substrate—to induce sizable extrinsic anisotropies between the different in-plane components of the resistivity tensor [4, 5]. To investigate this possibility in this work, we used standard lithographic techniques to pattern the same RuO₂/TiO₂(110) sample into four-point resistivity bridges with dimensions 55 μ m (length) \times 10 μ m (width) \times 24.2 nm (thickness), where the direction of current flow is confined (via lithography) to be aligned with specific crystallographic directions. In the course of performing the lithography, we noticed that the TiO₂ substrates became mildly conducting, possibly due to oxygen vacancies formed during ion milling, as has been reported to occur for SrTiO₃ [6]. Therefore, we annealed the wafer containing the patterned resistivity bridges in air at elevated temperatures until the

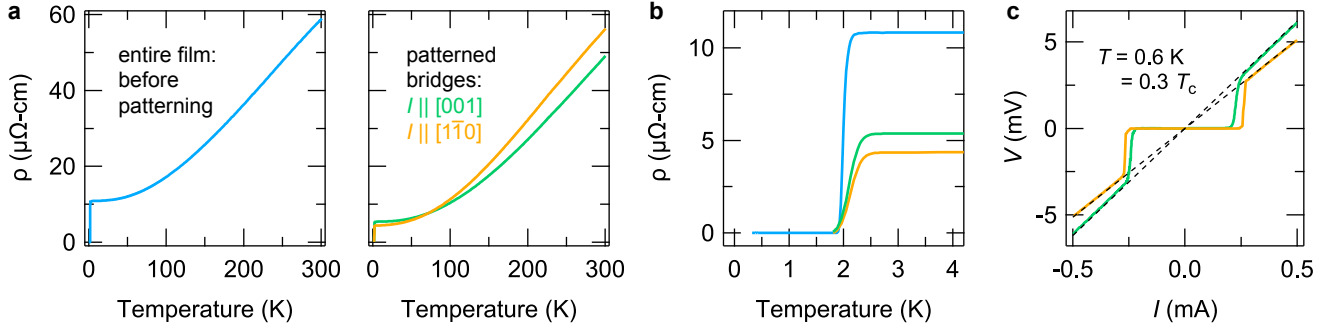
substrate again read open-circuit two-point resistances (> 100 M Ω); 2 hours at 500 $^\circ$ C was found to be sufficient.

The results of electrical measurements on these patterned resistivity bridges are shown by the green and orange traces in Supplementary Fig. 1. The temperature dependence of $\rho(T)$ is qualitatively consistent with the control measurements performed on the entire film before patterning, and the absolute magnitude of the resistivity anisotropies at 300 K and 4 K are both $< 20\%$. Furthermore, the superconducting $\rho(T)$ and $V(I)$ behavior does not depend strongly on the direction of current flow; this is contrary to what would be expected if the superconductivity arose purely from oriented structural defects.

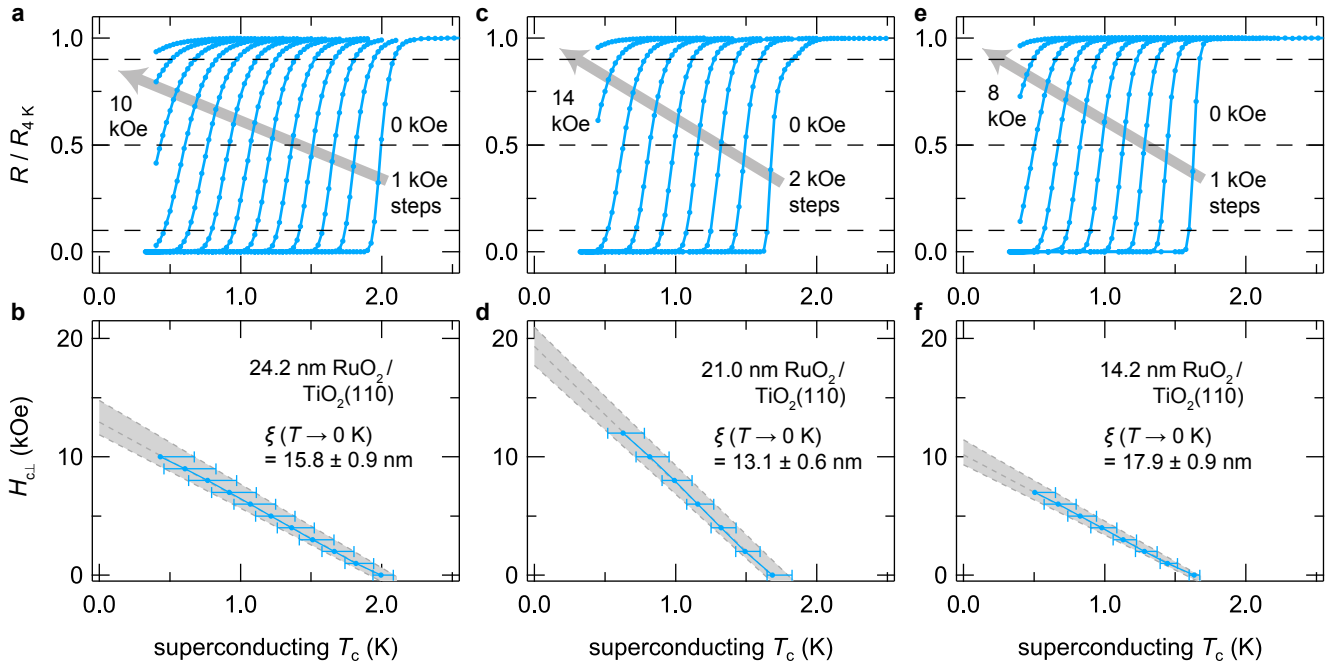
In Supplementary Fig. 1b, we ascribe the substantial decrease in low-temperature resistivities observed in the patterned resistivity bridge data relative to the entire film data to the aforementioned annealing involved in preparing the bridges. We confirmed on other RuO₂/TiO₂(110) samples not containing bridges that post-growth annealing in air generically causes the low-temperature values of ρ to drop, by as much as a factor of four. Because of these complications and additional uncertainties involved in lithographically patterning resistivity bridges on films on TiO₂ substrates, all other electrical transport data presented in the main text and in the supplementary information were acquired by wire bonding directly to the surfaces of as-grown samples that were not subject to any post-growth annealing treatments.

Supplementary Note 2: FITTING AND EXTRAPOLATION OF SUPERCONDUCTING UPPER CRITICAL FIELDS VERSUS TEMPERATURE

In Supplementary Fig. 2, we present the results of magnetoresistance measurements for three RuO₂/TiO₂(110) samples with different film thicknesses; the data in Supplementary Fig. 2a-b are reproduced from Fig. 1e-f of the main text. Each $R(T)$ trace was acquired at a discrete value of the externally applied magnetic field H_{\perp} (applied perpendicular to the surfaces of the films, along [110]) upon warming the samples up from base temperature



Supplementary Figure 1. **Electrical transport measurements exploring the anisotropy of the resistivity and superconductivity of a 24.2 nm thick $\text{RuO}_2/\text{TiO}_2(110)$ sample.** **a - b**, Zero-field $\rho(T)$ data measured on the entire as-grown film (blue) and after lithographically patterning four-point resistivity bridges (green and orange). **c**, Superconducting $V(I)$ curves measured on patterned resistivity bridges with the directions of current flow parallel to $[001]$ and $[1\bar{1}0]$.



Supplementary Figure 2. **Magnetoresistance measurements for three superconducting $\text{RuO}_2/\text{TiO}_2(110)$ samples with different film thicknesses.** Raw data traces in **a**, **c**, **e** are normalized to common values $R_{4\text{K}} \equiv R(T = 4\text{K}, H = 0\text{ kOe})$ for ease of visualization and analysis. The extracted scaling behavior of the upper critical fields versus superconducting $T_{c\text{s}}$ are plotted in **b**, **d**, **f**, along with the superconducting coherence length ξ corresponding to the extrapolated zero-temperature $H_{c\perp}$, cf. Supplementary Eq. (2). $T_{c\text{s}}$ are taken as the temperatures at which R crosses 50% of $R_{4\text{K}}$ (middle dashed lines in **a**, **c**, **e**); error bars in **b**, **d**, **f** indicate the temperatures at which R crosses the 90% and 10% thresholds of $R_{4\text{K}}$, respectively (top and bottom dashed lines in **a**, **c**, **e**).

through the superconducting transitions. All resistances are normalized to their zero-field values at 4 K, well above the superconducting transitions; since the normal-state $R(T, H)$ behavior of $\text{RuO}_2/\text{TiO}_2(110)$ in the absence of superconductivity is negligible in this regime of low temperatures and fields, the choice of a single normalization factor $R_{4\text{K}}$ for all data does not appreciably affect any of the results that follow. Because percolation effects

imply that resistive measurements of critical fields inherently contain some ambiguity about the definition and meaning of $H_{c\perp}$ relative to truly bulk-sensitive measurements of superconductivity [7], here we adopt the same convention employed in the main text: the temperature at which R crosses 50% of $R_{4\text{K}}$ is taken as T_c for the given $H_{c\perp}$, and the error bars on the extracted T_c are the temperatures at which R crosses the 90% and 10%

thresholds of $R_{4\text{K}}$, respectively [8].

While there are considerable quantitative discrepancies in the values of $H_{c\perp}$ and T_c for the different-thickness samples shown in Supplementary Fig. 2, the $H_{c\perp}(T_c)$ scaling behavior is remarkably linear for all samples, with no signs of $H_{c\perp}$ saturation down to reduced temperatures $T/T_c \approx 0.2 - 0.3$, unlike what is expected in, e.g., Werthamer-Helfand-Hohenberg (WHH) theory [9]. For example, evaluating the right hand side of the WHH expression

$$H_{c\perp}(T \rightarrow 0 \text{ K}) \leq -0.693 \left. \frac{dH_{c\perp}}{dT} \right|_{T=T_c} T_c \quad (1)$$

places upper bounds of 9.0, 13.5 and 7.1 kOe on $H_{c\perp}(T \rightarrow 0 \text{ K})$ for these three samples; however, the experimentally measured critical fields at 0.45 K (i.e., $T/T_c = 0.23, 0.27$ and 0.28) are already larger than these bounds: 10.0, 13.7 and 7.4 kOe, respectively. Therefore, to extrapolate $H_{c\perp}$ down to zero temperature, we performed linear Ginzburg-Landau-type fits to all available data and propagated the systematic uncertainties in the definition of $H_{c\perp}$ according to the gray dashed lines. The quoted zero-temperature values of the average in-plane superconducting coherence lengths $\xi(T \rightarrow 0 \text{ K})$ are obtained from the relation

$$\xi(T \rightarrow 0 \text{ K}) = \sqrt{\frac{\Phi_0}{2\pi\mu_0 H_{c\perp}(T \rightarrow 0 \text{ K})}}, \quad (2)$$

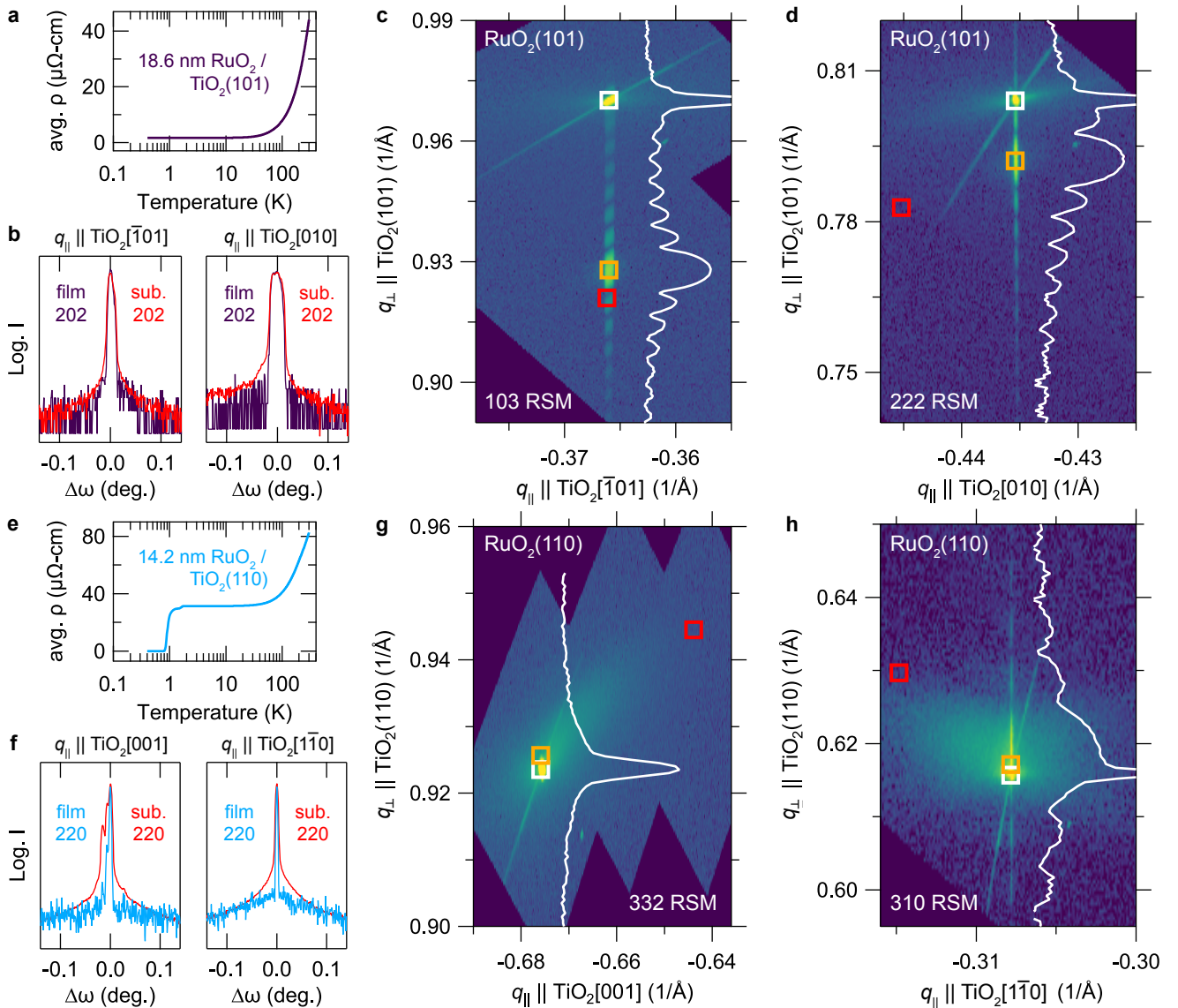
where Φ_0 is the superconducting flux quantum and μ_0 is the magnetic permeability of free space.

Notably, these values of $\xi(T \rightarrow 0 \text{ K})$ are less than values reported for traditional elemental superconductors with comparable T_c s by almost an order of magnitude, corresponding to critical fields that are $\approx 1 - 2$ orders of magnitude greater. While an explanation and understanding of these sizable critical field enhancements are beyond the scope of the present work, they are internally self-consistent with the large critical current densities noted in Fig. 1d of the main text and in Supplementary Fig. 1c. These results may motivate future real-space measurements of the superconducting condensate by scanning-probe techniques. In particular, an interesting question to address is whether the structural defects in $\text{RuO}_2(110)$ act as pinning sites for the vortices that form under applied fields, similar to what has been observed in numerous other thin-film superconductors [10], or whether the defects host regions of enhanced superfluid density that effectively act as barriers to vortex motion, akin to twin boundaries in bulk single crystals of iron-based superconductors [11, 12].

Supplementary Note 3: STRUCTURAL AND ELECTRICAL CHARACTERIZATION DATA FOR FILMS SYNTHESIZED ON DIFFERENTLY ORIENTED SUBSTRATES

In Supplementary Fig. 3, we include electrical characterization and more comprehensive lab-based x-ray diffraction (XRD) measurements for the $\text{RuO}_2(101)$ and $\text{RuO}_2(110)$ films of comparable thickness shown in Fig. 2a of the main text. Supplementary Fig. 3a,e show the zero-field $\rho(T)$ behavior for the two films: the 18.6 nm thick $\text{RuO}_2(101)$ film is non-superconducting down to $< 0.4 \text{ K}$ with a residual resistivity $\rho_0 < 1.7 \mu\Omega\text{-cm}$, whereas the 14.2 nm thick $\text{RuO}_2(110)$ film is superconducting at $T_c = 0.92 \pm \begin{smallmatrix} 0.21 \\ 0.07 \end{smallmatrix} \text{ K}$ with a residual resistivity $\rho_0 < 32 \mu\Omega\text{-cm}$. Supplementary Fig. 3b,f show rocking curves for the films overlaid on rocking curves for the TiO_2 substrates they were synthesized on: in all cases the coherent components of the film peaks exhibit narrow full width at half maximum (FWHM) values that are limited by the underlying substrate FWHM, as expected for isostructural film growths. In our studies we found that the rocking curve shapes and widths of the TiO_2 substrates supplied by CrysTec, GmbH can vary significantly depending on how the in-plane momentum transfer q_{\parallel} is oriented relative to the crystal axes of a given wafer, which may be due to the Verneuil process used to synthesize the crystals; to give some idea of the magnitude of this asymmetric mosaic spread, we show scans with q_{\parallel} oriented along azimuths separated by 90° for each sample.

In Supplementary Fig. 3c,d and Supplementary Fig. 3g,h we show off-specular (q_{\parallel}, q_{\perp}) reciprocal space maps (RSMs) for both samples in regions surrounding HKL Bragg peaks that have q_{\parallel} purely aligned with the crystallographic directions indicated in the labels on the horizontal axes. For reference, the peak positions that would be expected for the lattice parameters of bulk RuO_2 and bulk TiO_2 at 295 K [13, 14] are shown as red and white squares, respectively; the orange squares represent the central peak positions expected for commensurately strained RuO_2 thin films calculated using appropriately constrained density functional theory structural relaxations. To give a more quantitative sense of the logarithmic false color scale used here, the solid white lines overlaid on each plot represent the scattered intensity along the crystal truncation rods (CTRs)—i.e., the one-dimensional line cuts through the RSMs with q_{\parallel} equal to that of the substrate Bragg peaks. These results show that the 18.6 nm thick $\text{RuO}_2(101)$ film is coherently strained to the substrate along both in-plane directions, within the $\approx 0.1\%$ resolution of the measurements. The variable widths of the CTRs versus q_{\parallel} in different RSMs are an artifact of instrumental resolution effects—namely, the “tall” incident beam profile convolved with the scattering geometries used to measure each RSM—which we do not attempt to correct for in this work. On the other hand, the 14.2 nm thick $\text{RuO}_2(110)$ film is partially



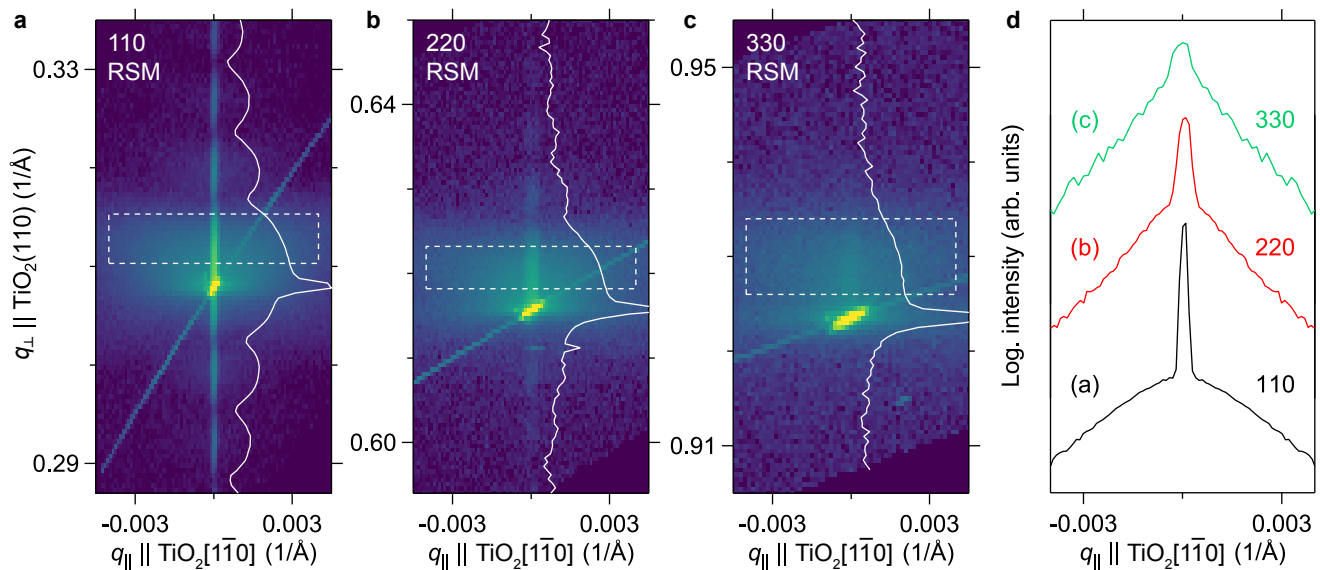
Supplementary Figure 3. **Electrical and structural characterization of (101)- and (110)-oriented RuO₂ thin films.**

a, Zero-field $\rho(T)$ (geometric mean) data for a non-superconducting 18.6 nm thick RuO₂(101) sample. **b**, Rocking curves for this sample, taken at 2θ values corresponding to the primary film and substrate 202 reflections. The FWHMs are 0.0081° with q_{\parallel} aligned along $[\bar{1}01]$ and 0.021° with q_{\parallel} along $[010]$. **c - d**, RSMs for this sample near the 103 and 222 reflections. Solid white lines are the scattering profiles along the CTRs. White, red, and orange squares represent the central peak positions expected for bulk TiO₂, bulk RuO₂ and commensurately strained RuO₂ thin films, respectively. The in-plane lattice mismatches of TiO₂ with bulk RuO₂ can be read off directly from the lateral offsets of the white and red squares: $+0.04\%$ (tensile) along $[\bar{1}01]$ in **c** and $+2.3\%$ along $[010]$ in **d**. **e - h**, Analogous electrical and structural data for a superconducting 14.2 nm thick RuO₂(110) sample. The rocking curve FWHMs at 220 are 0.0042° with q_{\parallel} aligned along $[001]$ (although there are clearly multiple peaks discernible in both the substrate and film curves) and 0.0036° with q_{\parallel} along $[1\bar{1}0]$. RSMs for RuO₂(110) at this film thickness show signatures of partial strain relaxation, because of the larger absolute levels of in-plane lattice mismatch with TiO₂: -4.7% along $[001]$ in **g** and $+2.3\%$ in **h**.

strain-relaxed, as evidenced by the more diffuse distribution of scattered intensity versus q_{\parallel} and less prominent finite-thickness fringes versus q_{\perp} along the CTRs. The diminished (or non-existent) contrast between thickness fringes in the CTRs for RuO₂(110) is likely a manifesta-

tion of crystalline disorder in the film interplanar spacings, since all (110)-oriented films have abrupt bounding interfaces—cf. the x-ray reflectivity data plotted in Supplementary Fig. 9a.

To further substantiate the partial strain relaxation



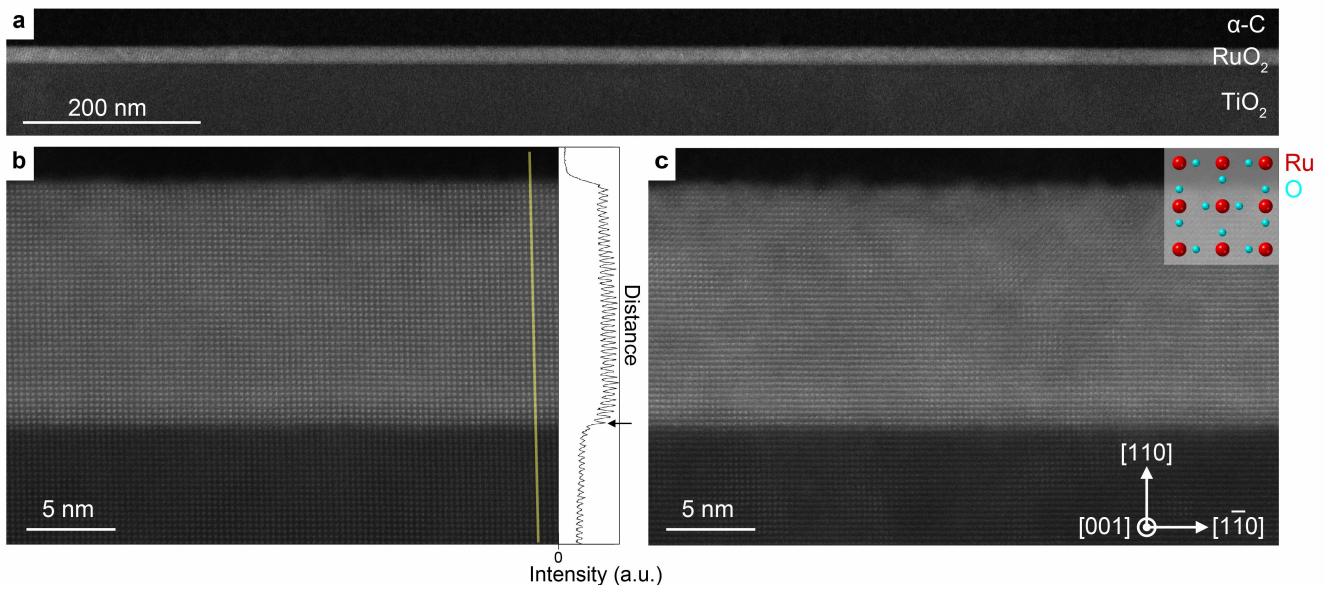
Supplementary Figure 4. **RSMs and rocking curves for a partially strain-relaxed 14.2 nm thick $\text{RuO}_2(110)$ sample.** **a - c**, RSMs measured near the 110, 220, and 330 Bragg reflections. Solid white lines are the scattering profiles along the specular ($q_{\parallel} = 0$) CTR. **d**, Line cuts of the intensities averaged over the dashed boxes in **a - c** show rocking curves with a two-component narrow plus broad structure characteristic of partially strain-relaxed epitaxial thin films. The in-plane momentum transfer q_{\parallel} is aligned with $\text{TiO}_2[1\bar{1}0]$ in all panels; similar results are obtained with q_{\parallel} along $\text{TiO}_2[001]$ (cf. Supplementary Figs. 9c, 10a).

observed in $\text{RuO}_2/\text{TiO}_2(110)$ samples, we measured RSMs around several Bragg peaks along the specular ($q_{\parallel} = 0$) CTR. Supplementary Fig. 4 summarizes the results of such measurements for the same 14.2 nm thick $\text{RuO}_2(110)$ sample for which off-specular RSMs are shown in Supplementary Fig. 3, which was also characterized by XRD and scanning transmission electron microscopy in Fig. 2 of the main text. By taking line cuts averaged over the dashed boxes—which span ranges of q_{\perp} where the measured intensities are predominantly due to scattering from the film—we obtained the three rocking curves plotted in Supplementary Fig. 4d. Each rocking curve shows a sharp central peak that is resolution-limited in width (or substrate-limited, cf. Supplementary Fig. 3b,f), superimposed on a much broader, nearly Lorentzian ($\text{FWHM} = 0.003 - 0.005 \text{ \AA}^{-1}$), component of the scattering that is also centered at $q_{\parallel} = 0$. Furthermore, the integrated intensity of the former coherent component of the scattering decays relative to that of the diffuse component as the magnitude of $|\mathbf{q}| = q_{\perp}$ increases in progressing from cut (a) to cut (c).

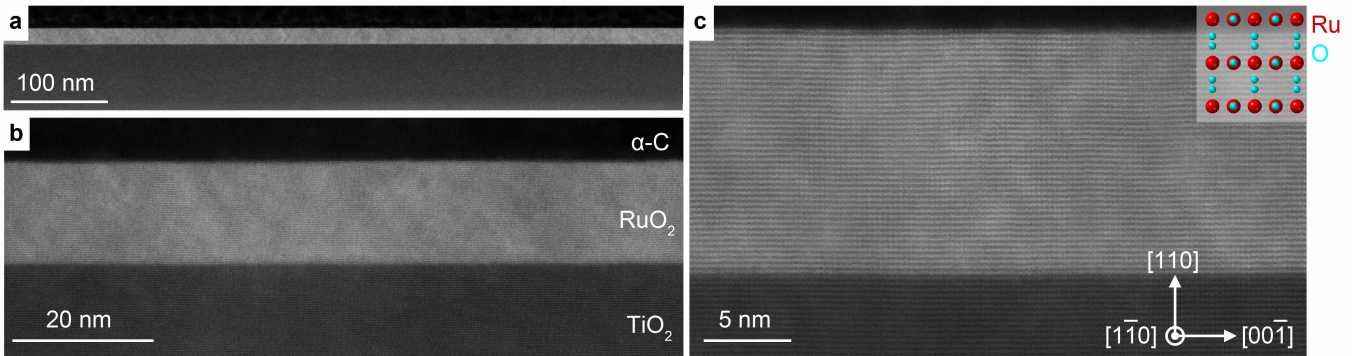
The non-vanishing intensity of the diffuse component in the film rocking curves, and the scaling behavior of how the total integrated intensity is distributed between the coherent and diffuse components as $|\mathbf{q}|$ is varied, are both completely consistent with published data for numerous epitaxial thin films grown on lattice-mismatched substrates where the films are thick enough to exhibit some form of strain relaxation [15–20]. In principle, by analyzing the diffuse scattering profiles around multi-

ple Bragg peaks with \mathbf{q} that project differently onto the Burgers vectors of the relevant misfit dislocations that relax the strain, one can obtain quantitative information on the types of dislocations that exist, the dislocation densities, etc. [21, 22]. We leave a more systematic analysis of this type to future synchrotron XRD studies, where the measurement noise floor is significantly lower and the strongly \mathbf{q} -dependent instrumental resolution effects observed here are mitigated by having a more point-like incident beam profile. We note, however, that the similar FWHM values of the diffuse scattering versus q_{\parallel} around the 110, 220, and 330 peaks imply that the structural defects responsible for this scattering are more translational in nature than rotational (which in typical mosaic crystals, produce rocking curves of constant *angular* widths) [15, 16]. Whether the inverses of these FWHM values for the fitted Lorentzians can be directly interpreted as the Fourier transform of a real-space correlation length (200–300 Å) depends on whether the film is in the limit of *weak (structural) disorder*, in the formalism of Refs. [16, 21].

Supplementary Figs. 5-6 show additional high-angle annular dark-field scanning transmission electron microscopy (HAADF-STEM) data from the same 14.2 nm thick $\text{RuO}_2(110)$ sample characterized in Fig. 2 of the main text and in Supplementary Figs. 3-4. Supplementary Fig. 5a shows that the morphology of the RuO_2 film is continuous and epitaxial to the TiO_2 substrate over the largest length scales probed. An intensity line profile taken along the growth direction (yellow line in



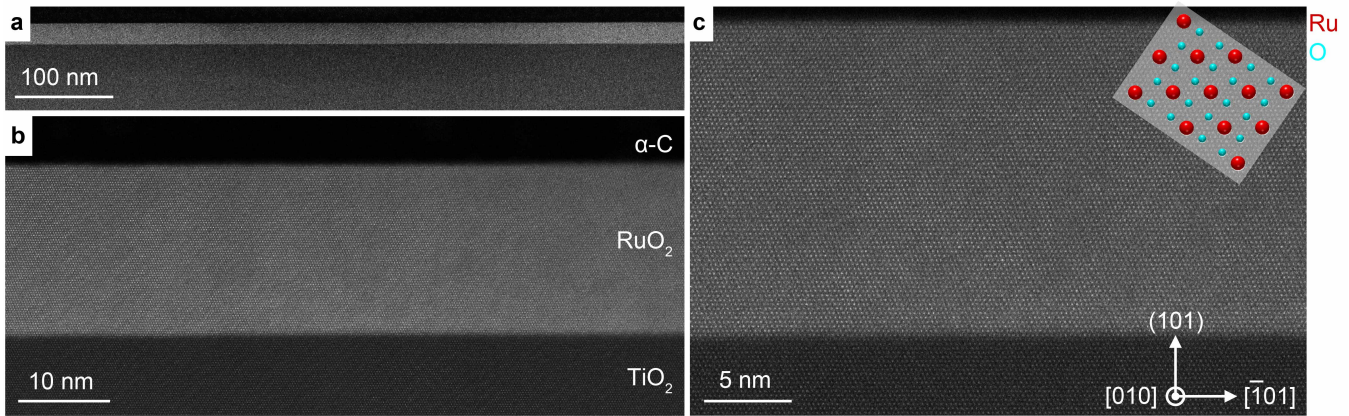
Supplementary Figure 5. **Variation in local crystalline quality across a superconducting 14.2 nm thick RuO₂(110) sample.** **a**, Z-contrast STEM image confirming continuous film growth across a micron-scale field of view. **b**, A crystallographically coherent region of the RuO₂(110) film from **a**. A line cut of the measured intensity across a continuous column of atoms along the growth direction (yellow line) shows an abrupt interface between TiO₂ and RuO₂, indicated by the black arrow. **c**, A relatively less-ordered region of the same film shown in the same projection, perpendicular to [001]_{rutile}. Inset shows the expected structure for this projection (not to scale).



Supplementary Figure 6. **HAADF-STEM structural characterization of a superconducting 14.2 nm thick RuO₂(110) sample in the higher strain direction.** Z-contrast STEM images acquired in [1 $\bar{1}$ 0] projection demonstrate the effects of the -4.7% compressive strain applied by the [001] axis of the TiO₂ substrate. **a**, Continuous film growth is observed across the full length of the STEM lamella, shown here without interruption over several hundreds of nanometers. **b**, Epitaxial film growth, as observed in the orthogonal projection (Supplementary Fig. 5), is again confirmed. **c**, Atomic-resolution image shows the crystalline quality of the strained RuO₂ film. Inset shows the expected structure for this projection (not to scale).

Supplementary Fig. 5b) confirms that an abrupt interface exists between TiO₂ and RuO₂. In particular, a sharp transition from lower intensity peaks in the substrate (Ti: $Z = 22$) to higher intensity peaks in the film (Ru: $Z = 44$) occurs over a region thinner than 1 nm surrounding the black arrow at the substrate-film interface; this indicates that any Ti/Ru chemical interdiffusion is minimal and cannot be the cause of the enhanced su-

perconductivity observed in RuO₂(110). At the lattice scale, we find that different regions from the same film exhibit varying degrees of crystalline coherence under the epitaxial strain applied by the TiO₂ substrate. The lateral in-plane direction imaged in Supplementary Fig. 5 is the [1 $\bar{1}$ 0] axis of the RuO₂ film, subject to +2.3% tensile strain from the TiO₂ substrate. Some regions, such as the one shown in Supplementary Fig. 5b, exhibit ex-



Supplementary Figure 7. **HAADF-STEM structural characterization of a non-superconducting $\text{RuO}_2(101)$ sample.** **a**, As in the superconducting $\text{RuO}_2(110)$ samples, continuous film growth is observed across the entire length of the STEM lamella. **b**, Epitaxial growth between the RuO_2 film and TiO_2 substrate is again confirmed. Here, however, the observed contrast is comparatively smooth across the film, without the clear signs of high strain observed in the $\text{RuO}_2(110)$ sample. **c**, Atomic-resolution STEM image demonstrating the high crystalline quality of the $\text{RuO}_2(101)$ sample. Inset shows the expected structure for this projection (not to scale).

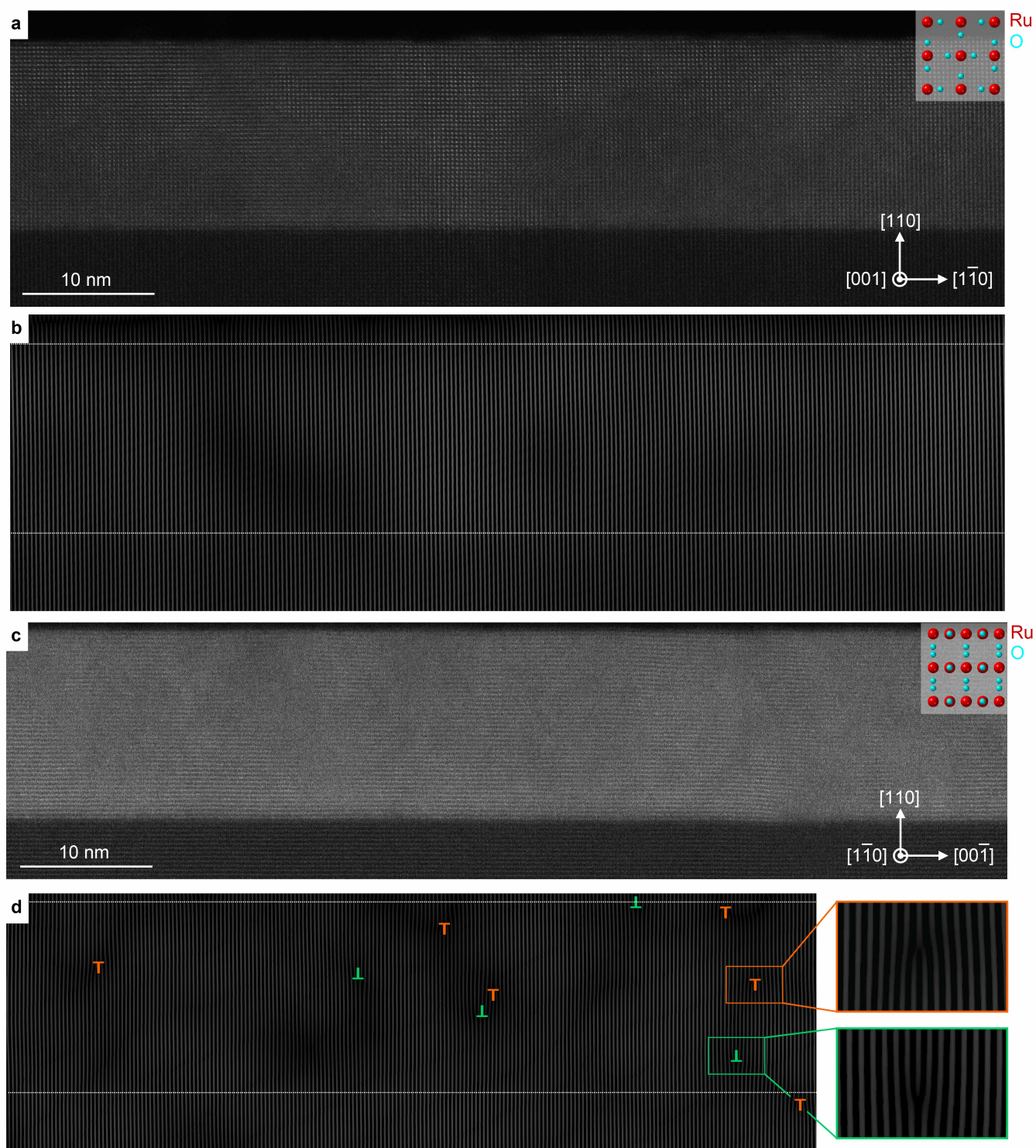
ceptionally clean crystalline quality: all of the atomic columns of Ru stack uniformly in the projection of the STEM image to produce highly ordered atomic contrast. In other regions of the same film, strain gradients in the film distort the RuO_2 lattice such that the columns of Ru atoms are slightly misaligned to the electron beam projection. This local misalignment of the lattice causes the apparent blurring and more mottled contrast of the STEM image seen in Supplementary Fig. 5c.

In Supplementary Fig. 6, the same sample is studied with HAADF-STEM imaging in the orthogonal projection direction. This orientation allows us to assess the crystalline response of the RuO_2 film along the $[001]$ in-plane direction, which is subject to a larger lattice mismatch with the TiO_2 substrate, -4.7% compressive strain. Again, Supplementary Fig. 6a confirms the continuous and epitaxial growth of the $\text{RuO}_2(110)$ thin film over the mesoscopic and macroscopic length scales relevant for interpreting the electrical transport data shown elsewhere in the manuscript. Effects of the large compressive strain along the in-plane direction of this projection are apparent in Supplementary Fig. 6a-b as characteristic V-shaped contrast in the RuO_2 film. Contributions from electron channeling in ADF-STEM imaging produces this bright/dark contrast in regions of local crystallographic strain; such contrast is a common signature of epitaxial lattice strain in many other oxide systems. Supplementary Fig. 6c shows the same structural response at atomic resolution, where—similar to Supplementary Fig. 5c—the apparent blurring of atomic columns arises from regions where the film lattice has been locally distorted.

Finally, for completeness we also performed HAADF-STEM measurements on the same non-superconducting 18.6 nm thick $\text{RuO}_2(101)$ film characterized in Fig. 1c and Fig. 2a of the main text and in Supplementary

Fig. 3. Z-contrast images of this sample are shown in Supplementary Fig. 7: the film is comparably continuous and epitaxial as the superconducting $\text{RuO}_2(110)$ films we have studied, without any signatures of extended defects or secondary phase inclusions that might otherwise alter its electrical properties. In good agreement with the XRD and electrical transport data shown in Supplementary Fig. 3, the $\text{RuO}_2(101)$ film exhibits more coherent crystalline order than the more drastically strained superconducting $\text{RuO}_2(110)$ films, even over relatively large fields of view as shown in Supplementary Fig. 7b. Supplementary Fig. 7c shows that the lattice remains largely defect-free down to the atomic scale.

The data presented in Supplementary Figs. 3-6 indicate that the crystal structures of superconducting $\text{RuO}_2(110)$ films are not commensurately strained to the TiO_2 substrates. To better visualize how this partial strain relaxation manifests in real space, we employed Fourier filtering of STEM images to find edge dislocations, following the techniques described in Ref. [23]. Specifically, in Supplementary Fig. 8a (Supplementary Fig. 8c) we plot an atomic-resolution HAADF-STEM image acquired in projection along $[001]$ (projection along $[1\bar{1}0]$) where the lateral in-plane direction is aligned with $[1\bar{1}0]$ ($[001]$, respectively). Supplementary Fig. 8b (Supplementary Fig. 8d) displays the Fourier component of this image with spatial frequencies $|q_{\parallel}| \approx 1/d_{1\bar{1}0}$ ($|q_{\parallel}| \approx 1/c$), which we obtained by computing the fast Fourier transform (FFT) of the image in Supplementary Fig. 8a (Supplementary Fig. 8c), and then taking the inverse FFT with the contributions of all spatial frequencies smoothly masked out except for those in a narrow region of q -space surrounding the noted $\pm q_{\parallel}$. The horizontal dashed lines in Supplementary Fig. 8b,d represent the boundaries of the film along the out-of-plane direction.



Supplementary Figure 8. **STEM imaging of edge dislocations in a superconducting $\text{RuO}_2/\text{TiO}_2(110)$ sample.** **a**, Atomic-resolution HAADF-STEM image in $[001]$ projection for the same 14.2 nm thick $\text{RuO}_2(110)$ film characterized elsewhere in the manuscript by STEM, x-ray diffraction, and electrical transport. **b**, Fourier-filtered version of the image in **a**, keeping only the components having $|q_{\parallel}| \approx 1/d_{1\bar{1}0}$ ($d_{1\bar{1}0} \approx 3.2 \text{ \AA}$). The horizontal dashed lines represent the boundaries of the film along the out-of-plane direction. The TiO_2 and RuO_2 lattices are continuously matched in plane over the entire 226-unit-cell-wide (73-nm-wide) field of view, without any dislocations. **c - d**, Same as in **a - b**, except in $[1\bar{1}0]$ projection and isolating the Fourier component of the image having $|q_{\parallel}| \approx 1/c$ ($c \approx 3.0 \text{ \AA}$). Nearly equal numbers of edge dislocations are observed in **d** with Burgers vectors of $-\mathbf{c}$ (orange) and $+\mathbf{c}$ (green), respectively, across a 204-unit-cell-wide (61-nm-wide) field of view. The insets on the right side of panel **d** are magnified by 3 \times .

In this representation, edge dislocations appear as topological defects in the otherwise continuous vertical streaks appearing in Supplementary Fig. 8b,d. These vertical streaks are formally the lattice points of the film and substrate crystal structures, blurred into streaks along the out-of-plane direction because we discard any high-spatial-frequency information about out-of-plane correlations of the electron density (i.e., $q_{\perp} \not\approx 0$) when computing the inverse FFTs. Hereafter we loosely refer to these streaks as *atomic columns*, since the contrast in these HAADF-STEM data arises predominantly from electron scattering by the atomic cores with larger Z (i.e., Ti and Ru). Dislocations indicated by green markers add one atomic column to the number of columns that exist in layers beneath it (thus relaxing tensile strain in the lateral direction), whereas dislocations indicated by orange markers remove one atomic column to the number of columns that exist in layers beneath it (thus relaxing compressive strain in the lateral direction). Therefore, a fully strain-relaxed film of RuO₂/TiO₂(110) would show a collection of only green (only orange) dislocations accumulated at the substrate-film interface in Supplementary Fig. 8b (Supplementary Fig. 8d, respectively). The dislocation densities expected in this fully strain-relaxed scenario would be 1 per every $1/0.023 \approx 43$ vertical streaks for green dislocations in Supplementary Fig. 8b, and 1 per every $1/0.047 \approx 21$ vertical streaks for orange dislocations in Supplementary Fig. 8d.

In marked contrast to this behavior, zero dislocations are observed across a 226-unit-cell-wide field of view in Supplementary Fig. 8b. Furthermore, although a significantly higher density of dislocations is present across the 204-unit-cell-wide field of view in Supplementary Fig. 8d, there are nearly equal numbers of edge dislocations having Burgers vectors of $-\mathbf{c}$ (orange) and $+\mathbf{c}$ (green), respectively, and the dislocations are rather uniformly distributed throughout the entire thickness of the film. These observations imply that throughout a sizable volume fraction of the superconducting film, the crystal structure is, on average, much closer to the commensurately-strained limit than to the fully-relaxed limit. We note that this agrees well with the distribution of x-ray scattering intensities plotted in the RSMs for this sample and others in Supplementary Figs. 9-10. Based on these data, we suggest that it is appropriate to consider the local strain gradients that inevitably accompany the nucleation of dislocations in RuO₂(110) to be sample-dependent perturbations to significantly larger average components of the substrate-imposed strain fields that are present throughout all films shown in the manuscript. Because superconductivity is an essentially mean-field phenomenon, we believe that the latter average components of the strain fields in RuO₂(110) are the key ingredients for stabilizing superconductivity with transition temperatures at least an order of magnitude larger than in bulk RuO₂; finer details of the local strain gradients probably determine finer details of the superconductivity, such as the exact sample-dependent T_c s mea-

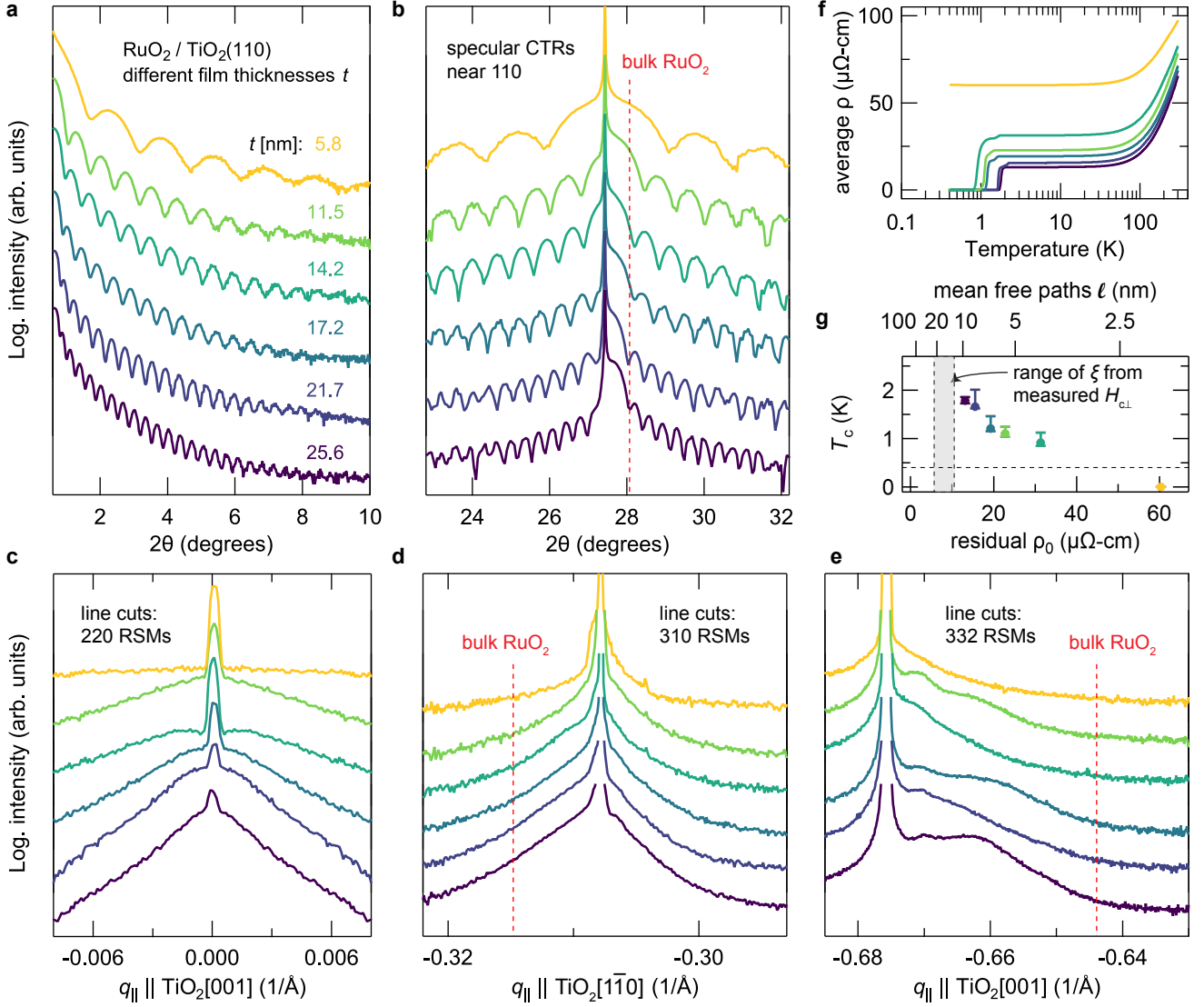
sured by non-bulk-sensitive probes of superconductivity, such as resistivity. Since our platform for applying strain enables scanning-probe measurements of the superconducting condensate, future experiments may be able to provide direct experimental evidence to support these general expectations of mesoscale or nanoscale strain inhomogeneity resulting in spatially inhomogeneous superconductivity [24].

Supplementary Note 4: STRUCTURAL AND ELECTRICAL CHARACTERIZATION DATA FOR RuO₂(110) FILMS OF DIFFERENT THICKNESSES

Figure 2b-c of the main text shows that the superconducting T_c s of RuO₂ thin films synthesized on TiO₂(110) substrates depend sensitively on the thickness of the films, t . We do not purport to completely understand this empirical observation, but Supplementary Figs. 9-10 include several additional pieces of structural and electrical characterization data for this same thickness series of RuO₂(110) samples that constrain potential explanations.

In Supplementary Fig. 9a-b, we plot x-ray reflectivity (XRR) data taken at low incident angles, and XRD data taken near the 110 Bragg peaks of the film and substrate, both acquired along the specular CTRs using Cu-K α radiation. Finite-thickness fringes are present over a wide range of angles in both data sets, evidencing (from reflectivity) atomically abrupt interfaces of the films with the substrates and with vacuum, and (from diffraction) comparable levels of crystallinity along the out-of-plane direction across samples. Furthermore, the spacings between secondary maxima on either side of the primary film Bragg peaks in XRD match the spacings between the low-angle XRR fringes, suggesting that the crystal structures of all films are essentially homogeneous along the out-of-plane direction. The film thicknesses t listed in Fig. 2b-c of the main text and in Supplementary Figs. 9-10 are obtained by directly fitting the XRR data in Supplementary Fig. 9a using a genetic algorithm, which yields sub-nanometer roughnesses in all cases in the refined models.

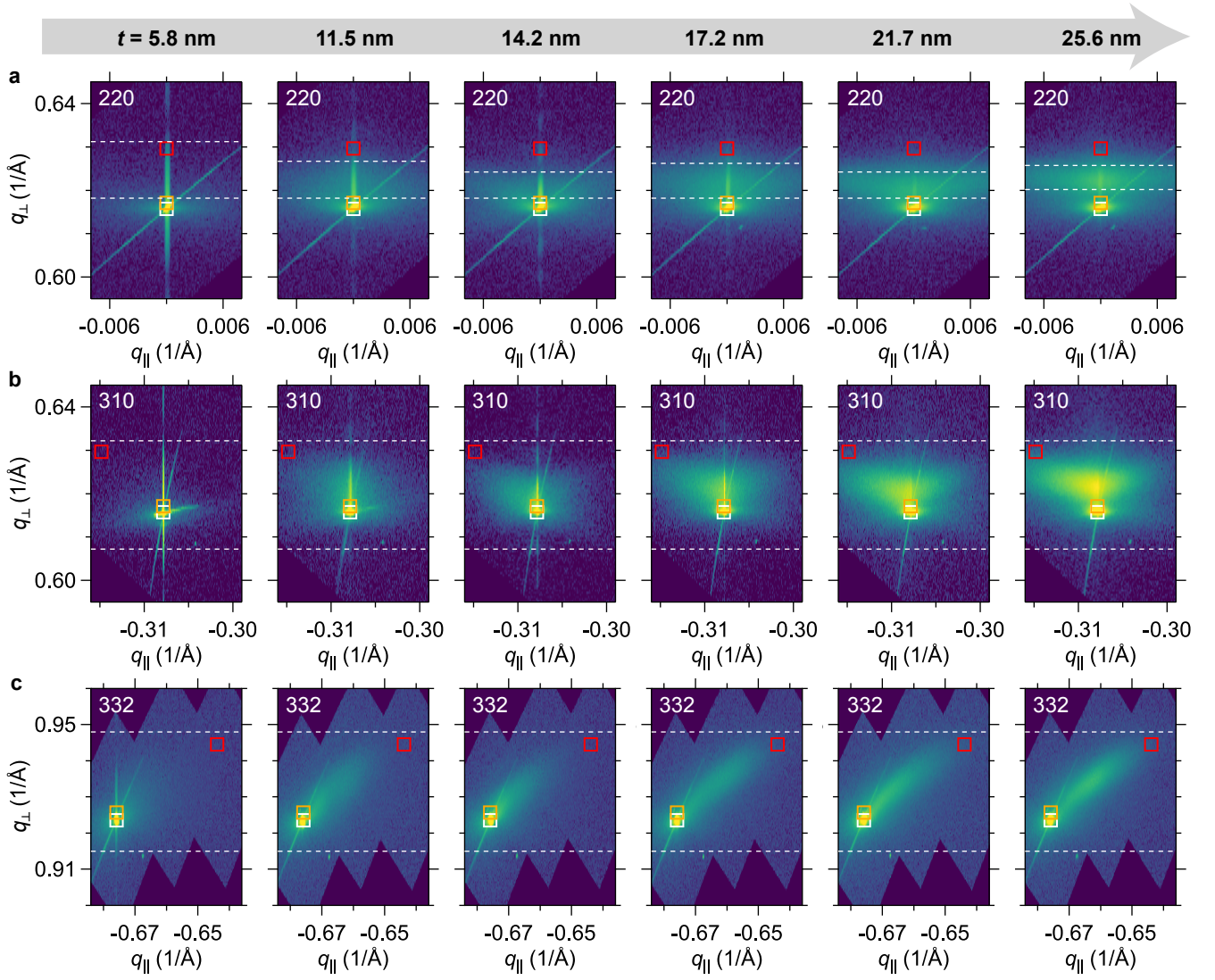
Given that there are no obvious differences in film morphology or out-of-plane crystallinity between RuO₂(110) samples with different t , an alternative explanation that may account for the thickness-dependent superconducting T_c s is the proliferation of misfit dislocations in thicker films that progressively relax the epitaxial—i.e., in-plane—strains; in this scenario, it may be that partially strain-relaxed RuO₂(110) films have higher (average) superconducting T_c s compared with fully commensurately strained RuO₂(110) films. To investigate this possibility, in Supplementary Fig. 9c-e we plot line cuts of the intensity versus q_{\parallel} extracted from RSMs near the 220, 310, and 332 Bragg reflections of the RuO₂(110) thin films and TiO₂ substrates. The raw data for all



Supplementary Figure 9. **Evolution of crystal structure and electrical transport behavior as a function of film thickness for RuO₂/TiO₂(110).** **a**, X-ray reflectivity and **b**, x-ray diffraction data along the specular CTR show comparable levels of flatness and crystalline order along the out-of-plane direction for all samples. **c - e**, Average line cuts versus q_{\parallel} through the 220, 310, and 332 RSMs (fully \mathbf{q} -resolved data are shown in Supplementary Fig. 10) indicate that all samples with $t > 5.8$ nm exhibit partial strain relaxation. **f - g**, Zero-field $\rho(T)$ data show that thinner films generally have higher residual resistivities ρ_0 and lower superconducting T_c s. T_c s in **g** are taken as the temperatures at which $\rho(T)$ crosses 50% of the normal-state ρ_0 , and error bars indicate the temperatures at which $\rho(T)$ crosses 90% and 10% of ρ_0 , respectively. The horizontal dashed line in **g** represents the base temperature attainable in our cryostat (0.4 K), and the gray-shaded region indicates the range of superconducting coherence lengths ($\xi = 12 - 22$ nm) extracted from magnetoresistance measurements of the upper critical fields for ten different RuO₂(110) thin films. Comparisons of these ξ with the mean free paths ℓ (top axis of **g**) that correspond to the measured ρ_0 (bottom axis of **g**) indicates that superconductivity persists in the dirty limit $\ell < \xi$.

RSMs are plotted in Supplementary Fig. 10 using logarithmic false color scales; the line cuts in Supplementary Fig. 9c-e are averaged over the ranges of q_{\perp} between the dashed white lines in Supplementary Fig. 10. All of the samples except the thinnest film exhibit diffuse scattering surrounding the CTRs, indicating that partial strain relaxation onsets between film thicknesses of 5.8 nm and 11.5 nm for the growth conditions used in this work to

synthesize RuO₂/TiO₂(110) samples. Since the in-plane lattice mismatches between RuO₂ and TiO₂ are highly anisotropic for the (110) orientation, it might also be expected that the substrate-imposed compressive strain along [001] (−4.7%) starts to relax at smaller film thicknesses than the tensile strain along [1 $\bar{1}$ 0] (+2.3%) [17, 19]. The off-specular RSMs in Supplementary Fig. 10b-c qualitatively agree with this expectation, inasmuch as finite-



Supplementary Figure 10. **RSMs for RuO₂/TiO₂(110) samples with different film thicknesses, t .** **a**, RSMs along the specular CTR near the 220 Bragg reflections for films with increasing t , moving from left to right. q_{\parallel} is aligned with [001] in all panels, although the phenomenology is similar with q_{\parallel} along [1 $\bar{1}$ 0], cf. Supplementary Fig. 4. **b**, Thickness-dependent RSMs near the off-specular 310 Bragg reflections where q_{\parallel} is purely along [1 $\bar{1}$ 0]. **c**, Same as **b**, but near the 332 Bragg reflections where q_{\parallel} is purely along [001]. White, red, and orange squares represent the central peak positions expected for bulk TiO₂, bulk RuO₂, and commensurately strained RuO₂(110), as in Supplementary Fig. 3. The line cuts plotted in Supplementary Fig. 9c-e are averaged over the ranges of q_{\perp} of the RSMs between the horizontal white dashed lines.

thickness fringes can still be observed along the CTRs in the RSMs near 310 for films up to at least $t = 17.2$ nm, whereas only the $t = 5.8$ nm film shows a contribution to the coherent CTR scattering in the RSMs near 332 that clearly rises above the contributions of the substrate.

Although signatures of scattering from partially strain-relaxed RuO₂(110) are manifestly present in the data for all of the superconducting samples in Supplementary Fig. 9—namely, broader distributions of intensity versus q_{\parallel} that asymmetrically gain weight towards the positions expected for bulk RuO₂ as the film thickness increases—it remains somewhat ambiguous whether this data can be

interpreted in a straightforward manner to gain insight into what levels of strain optimize the superconducting T_c s in RuO₂. Strain relaxation in oxide thin films often occurs inhomogeneously, with a mixture of commensurately strained and partially relaxed material [25]. Indeed, examining the transport data for these same samples in Fig. 2b of the main text and in Supplementary Fig. 9f, it is tempting to ascribe the multi-stage behavior of the superconducting transitions to temperature-dependent Josephson coupling of regions of the films under different amounts of strain with correspondingly different “local” T_c s; similar behavior has been described

theoretically [26] and observed experimentally in patterned niobium islands on gold substrates [27]. However, because of the close proximity of the substrate Bragg peaks along q_{\perp} ($d_{110} = 3.248 \text{ \AA}$) with the positions expected for commensurately strained $\text{RuO}_2(110)$ ($d_{110} = 3.241 \text{ \AA}$), it is difficult to disentangle their respective contributions to the total scattering observed in XRD.

Despite these complications in quantitatively analyzing the XRD results, we can use the values of t obtained from XRR to plot the normalized resistance versus temperature curves from Fig. 2b of the main text in terms of absolute resistivities, as shown in Supplementary Fig. 9f. From these data, a robust correlation between the superconducting T_c s and the residual resistivities ρ_0 immediately becomes apparent, as displayed in Supplementary Fig. 9g. As noted in the main text, this correlation may suggest that the primary effect of reducing t is to enhance the relative importance of elastic scattering off disorder near the substrate-film interfaces, which is known to decrease T_c in numerous families of thin-film superconductors, both conventional [28] and unconventional [29]. It is largely outside the scope of this paper to contribute meaningful data to ongoing research efforts investigating the mechanism underlying thickness-induced suppressions of T_c that are ubiquitously observed for superconducting films in the two-dimensional limit [30]; however, in passing we note that the residual resistivity ($\rho_0 = 60 \mu\Omega\text{-cm}$) of the thinnest ($t = 5.8 \text{ nm}$) non-superconducting ($T_c < 0.4 \text{ K}$) $\text{RuO}_2(110)$ film shown in Supplementary Fig. 9 corresponds to a sheet resistance of $R_s = \rho_0/t = 0.10 \text{ k}\Omega/\square$. This value of R_s is about 60 times less than the Cooper pair quantum of resistance $h/(2e)^2 = 6.45 \text{ k}\Omega/\square$ that was empirically noted to separate insulating from superconducting ground states in ultrathin films of numerous elemental metals [31, 32]; this indicates that quantitatively different physics is likely operative here in suppressing T_c , which may place ultrathin films of $\text{RuO}_2(110)$ in closer proximity to the *anomalous metal* regime that was shown to occur at weaker levels of disorder in Ref. [33].

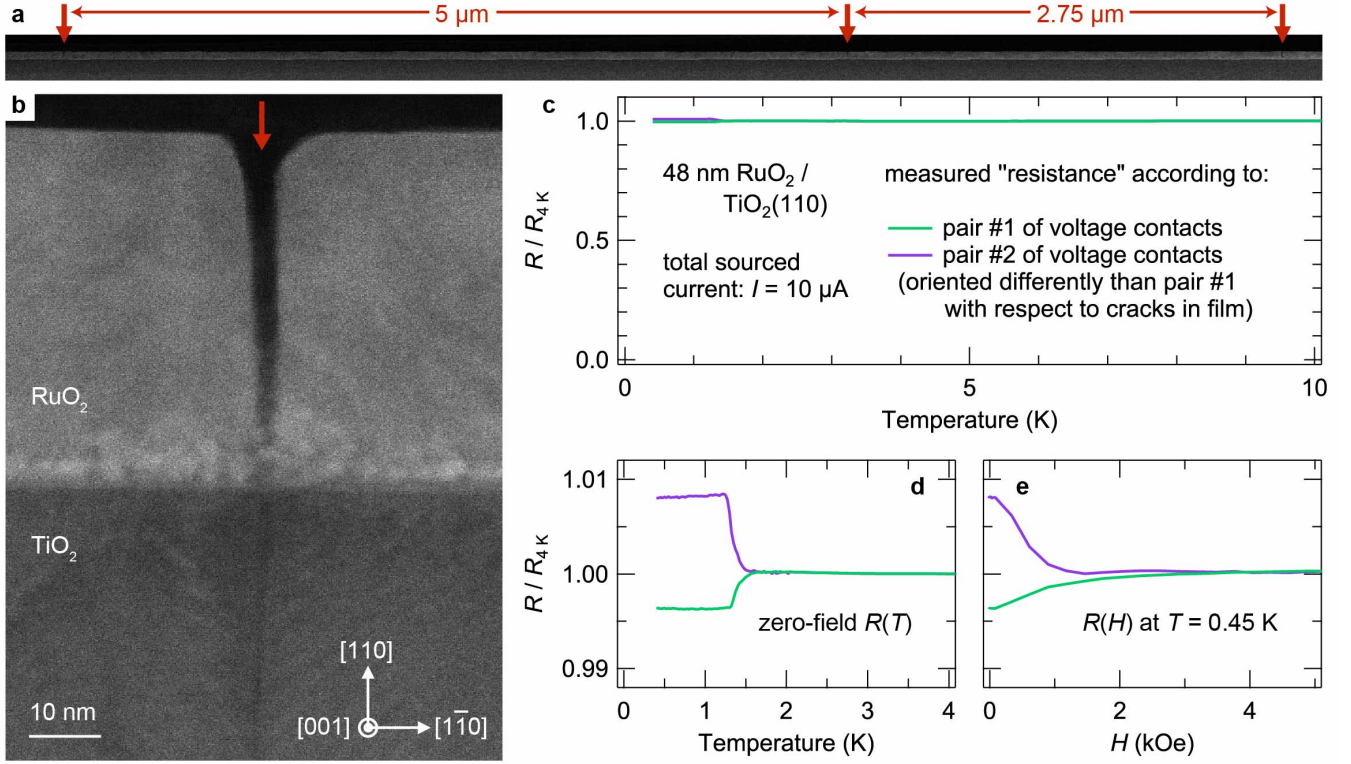
We believe that identifying the exact mechanism underlying the strain-stabilized superconductivity in $\text{RuO}_2(110)$ is also well beyond the scope of the current paper. Phase-sensitive measurements of the superconducting order parameter—and/or momentum-resolved measurements of the superconducting gap magnitude—are notoriously challenging in multi-band materials with small (sub-meV) gaps, and a definitive answer to whether the pairing is (un)conventional will have to wait until such data become available. With that qualification in mind, it is natural to consider whether the T_c versus ρ_0 behavior displayed in Supplementary Fig. 9g can shed any light on the answer to this question. To address this possibility, we need to convert measured properties of the normal-metal and superconducting states into comparable characteristic length scales. In unconventional low-temperature superconductors with sign-

changing order parameters, such as Sr_2RuO_4 [34], superconductivity is completely suppressed by non-magnetic impurity scattering whenever the normal-state mean free path ℓ is comparable with the clean-limit superconducting coherence length ξ_0 —i.e., $T_c \rightarrow 0 \text{ K}$ if $\ell \approx \xi_0$. In conventional superconductors, by contrast, superconductivity persists even in the dirty limit $\ell \ll \xi_0$.

On the top horizontal axis of Supplementary Fig. 9g, we indicate approximate values of ℓ corresponding to the measured values of ρ_0 on the bottom horizontal axis; these numbers are computed following the analysis of Glassford et al. [3], who used the DFT-computed plasma frequencies and Fermi velocities for bulk RuO_2 to obtain $\ell [\text{nm}] = 3.6 \cdot 35/\rho [\mu\Omega\text{-cm}]$. Because of various uncertainties implicit in these estimations, we neglect any strain-dependent changes in Fermiology that will, of course, quantitatively renormalize the precise relationship between ℓ and ρ for $\text{RuO}_2(110)$. To compare with ℓ , we also include a gray-shaded region on Supplementary Fig. 9g corresponding to the range of average in-plane superconducting coherence lengths ξ we extracted experimentally from magnetoresistance measurements of the perpendicular upper critical magnetic fields $H_{c\perp}$ for ten different superconducting $\text{RuO}_2(110)$ samples, following the procedures detailed in Supplementary Note 2. As noted previously, these values of ξ likely represent a lower bound for what the clean-limit ξ_0 would be in the absence of extrinsic defects in the films that impede vortex motion. In any case, we find that superconductivity robustly persists in $\text{RuO}_2(110)$ even when $\ell < \xi < \xi_0$; for example, the samples shown here with $T_c = 0.9 - 1.8 \text{ K}$ have measured residual resistivities corresponding to mean free paths $\ell = 4.0 - 9.6 \text{ nm}$, which are all less than the range of measured superconducting coherence lengths, $\xi = 12 - 22 \text{ nm}$. Therefore, whatever the superconducting pairing mechanism is in $\text{RuO}_2(110)$, these empirical considerations demonstrate that it is rather insensitive to defect scattering.

Conceptually, perhaps the most straightforward test of our proposal that substrate-imposed strains are an essential ingredient in stabilizing superconductivity in $\text{RuO}_2(110)$ would be to perform electrical transport measurements for a thick $\text{RuO}_2(110)$ film where the epitaxial strains are almost completely relaxed. In reality, however, such efforts are complicated by the observation that the +2.3% tensile strain along $[1\bar{1}0]$ is not released in sufficiently thick films of $\text{RuO}_2(110)$ by the nucleation of misfit dislocations; instead, cracks form in such samples (in our studies, for $t \gtrsim 30 \text{ nm}$) that propagate through the entire thickness of the film and even tens of nanometers into the substrate.

In Supplementary Fig. 11a-b, we show HAADF-STEM images of such oriented micro-cracks for the same 48 nm thick $\text{RuO}_2(110)$ film characterized by ARPES and LEED in Fig. 4 of the main text and in Supplementary Figs. 14-15. Although these images evidence strong interfacial bonding between film and substrate—which is certainly crucial to maintain high levels of strain throughout



Supplementary Figure 11. **Structural and electrical characterization of a cracked 48 nm thick RuO₂/TiO₂(110) sample.** **a**, HAADF-STEM image of the sample over a wide field of view, showing an anisotropically oriented network of cracks (red arrows) each separated by a few microns. Note that the cracks appear only in projection view along [001]—i.e., perpendicular to $[1\bar{1}0]$, which is the in-plane direction of the film under tensile strain. **b**, Magnified image of a crack from **a**. **c**, Zero-field “resistance” versus temperature data for two different pairs of voltage contacts oriented differently with respect to the network of cracks visualized in **a** and **b**. **d**, Same $R(T)$ data as in **c**, plotted on a greatly expanded vertical scale. **e**, “Resistance” versus externally applied magnetic field data for the pairs of voltage contacts from **c** and **d**, taken at fixed temperature $T = 0.45$ K.

the thinner RuO₂(110) films we characterize elsewhere in the manuscript—the strongly anisotropic nature of the cracks makes the distribution of current flow through such samples extremely non-uniform. Accordingly, putative measurements of electrical “resistance” $R(T, H)$ displayed in Supplementary Fig. 11c-e should be more pedantically interpreted as the voltage difference measured between two voltage contacts, divided by the total current sourced through two other contacts placed elsewhere on the film. Unsurprisingly, the results thus obtained for R depend in an essential way on the orientation of the voltage contacts relative to the cracks in the film: in Supplementary Fig. 11c-d we observe either a downturn (green trace) or upturn (purple trace) in the apparent R as the temperature is decreased below $T_c = 1.3 - 1.5$ K, followed by plateaus at lower temperatures. In Supplementary Fig. 11e, we show that these temperature-induced anomalies in R can be suppressed in both cases by applying small magnetic fields $H_{c\perp} < 3$ kOe at fixed $T = 0.45$ K, confirming that they result from (inhomogeneous) patches of superconductivity. Irrespective of whether the measured R decreases or

increases at (T_c, H_c) , we emphasize that the fractional changes in resistance induced by superconductivity in this 48 nm thick RuO₂(110) film are less than 1% of the residual normal-state resistances R_{4K} , in marked contrast to the full 100% drops to zero resistance exhibited by all thinner, more highly strained, uncracked RuO₂(110) films shown in other figures.

Supplementary Note 5: DENSITY FUNCTIONAL THEORY CALCULATIONS

Structural relaxations

One of the central themes of this work is the exploration of strain-induced changes to the electronic structure in epitaxial thin films of RuO₂ subject to biaxial epitaxial strains imposed by differently oriented rutile TiO₂ substrates. To model this situation computationally within the framework of density functional theory (DFT), we started by using the Vienna Ab Initio Software Package [35, 36] to perform full structural

relaxations (of lattice parameters and internal coordinates) to minimize the DFT + U -computed total energy of RuO₂ in the ideal tetragonal rutile crystal structure (space group #136, $P4_2/mnm$). Structural relaxations employed the same exchange-correlation functional and calculational parameters as for the DFT + U ($U = 2$ eV) calculations described in the Methods section of the main text, and forces were converged to < 1 meV/Å.

Throughout the main text and supplementary information, we refer to DFT results for this minimum energy structure as “bulk RuO₂”. The actual lattice parameters for this structure, ($a_{\text{bulk}} = 4.517$ Å, $c_{\text{bulk}} = 3.130$ Å), overestimate the experimentally measured lattice parameters at 295 K for RuO₂ single crystals ($a = 4.492$ Å, $c = 3.106$ Å) by $< 1\%$, due to well-established deficiencies of the generalized gradient approximation. With the former as the bulk reference structure, we then simulated biaxial epitaxial strains to (110)-oriented TiO₂ substrates by performing constrained structural relaxations for RuO₂ in which the in-plane lattice parameters $c = (1 - 0.047) \times c_{\text{bulk}}$ and $d_{1\bar{1}0} = (1 + 0.023) \times d_{1\bar{1}0, \text{bulk}}$ were held fixed, while the out-of-plane lattice constant d_{110} and all other internal coordinates of the structure were allowed to relax so as to minimize the total energy. The fixed compression and expansion of c and $d_{1\bar{1}0}$, respectively, correspond to the experimentally measured lattice mismatches between TiO₂ and RuO₂ single crystals at 295 K [13, 14].

Within this scheme, DFT + U predicts that commensurately strained RuO₂(110) thin films will have an out-of-plane lattice constant $d_{110} = (1 + 0.017) \times d_{110, \text{bulk}}$, which compares reasonably well with the 2.0% expansion of d_{110} measured experimentally on a 5.8 nm thick RuO₂(110) film. Because the splitting of d_{110} and $d_{1\bar{1}0}$ in strained RuO₂(110) breaks the non-symmorphic glide plane symmetry of the parent rutile structure, we used a base-centered orthorhombic structure (space group #65, $Cmmm$) with lattice constants of $c \times 2d_{1\bar{1}0} \times 2d_{110}$ for DFT simulations of RuO₂(110). The primitive unit cell of this $Cmmm$ structure contains the same number of atoms as the parent rutile unit cell, so there is no apparent doubling and/or folding of the bands in spaghetti plots that compare the bandstructures of RuO₂(110) and bulk RuO₂, such as in Supplementary Fig. 12 or Fig. 4a of the main text.

To simulate the electronic structure of commensurately strained (101)-oriented RuO₂ thin films, we adopted a slightly different approach, since it is not straightforward to perform constrained structural relaxations with DFT in such a low-symmetry situation. Specifically, we took the rutile b axis to be under +2.3% tension, i.e. $b = (1 + 0.023) \times b_{\text{bulk}}$, as dictated by the lattice mismatch of RuO₂ with TiO₂ along this direction (cf. Supplementary Fig. 3d). On the other hand, the lengths of the rutile a and c axes are free to adjust their lengths, but are subject to the simultaneous constraints:

$$\sqrt{a^2 + c^2} = \sqrt{(a_{\text{TiO}_2})^2 + (c_{\text{TiO}_2})^2} = 5.464 \text{ Å} \quad (3)$$

$$|\mathbf{q}_{202}| = \sqrt{\left(\frac{2}{a}\right)^2 + \left(\frac{2}{c}\right)^2} = 0.792 \text{ Å}^{-1} \quad (4)$$

$$|\mathbf{q}_{103}| = \sqrt{\left(\frac{1}{a}\right)^2 + \left(\frac{3}{c}\right)^2} = 0.998 \text{ Å}^{-1} \quad (5)$$

$$|\mathbf{q}_{402}| = \sqrt{\left(\frac{4}{a}\right)^2 + \left(\frac{2}{c}\right)^2} = 1.114 \text{ Å}^{-1}. \quad (6)$$

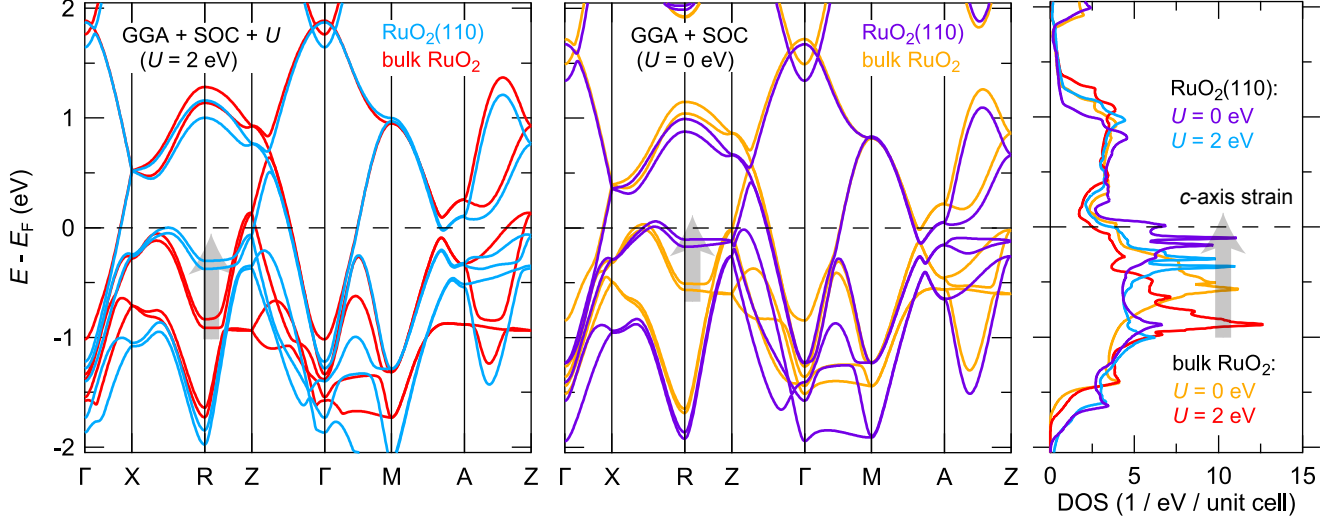
Supplementary Eq. (3) ensures that the film is lattice matched to the TiO₂ substrate along the $[\bar{1}01]$ in-plane direction (cf. Supplementary Fig. 3c), and Supplementary Eqs. (4)-(6) ensure that the d -spacings for the $HKL = 202, 103,$ and 402 Bragg reflections reproduce the values we measured experimentally for a commensurately strained RuO₂(101) film in Fig. 2a of the main text, in Supplementary Fig. 3c, and in analogous RSM data taken around 402 (a proper, i.e. highly overconstrained, lattice constant refinement would of course include data for many more reflections). Note that in deriving these equations, we assumed for simplicity that the angle between the rutile a and c axes remains 90° in epitaxially strained films; small deviations away from this limit should be expected in reality, since this orthogonality is not guaranteed by any symmetry or constraint of the system. Nonetheless, finding the best-fit solution to Supplementary Eqs. (3)-(6) gives lattice constants of ($a = 4.501$ Å, $c = 3.077$ Å) in absolute units; dividing through by the experimentally measured lattice constants of bulk RuO₂ yields $a = (1 + 0.002) \times a_{\text{bulk}}$ and $c = (1 - 0.009) \times c_{\text{bulk}}$ as appropriately scaled inputs for DFT simulations. With $a \neq b \neq c$ and all angles between the primitive unit cell translations equal to 90° , the crystal structure for RuO₂(101) DFT simulations was taken as the primitive orthorhombic space group #58, $Pnmm$. Supplementary Table 1 summarizes all parameters of the crystal structures used in DFT simulations for bulk RuO₂, RuO₂(110), and RuO₂(101).

Effects of adding + U

In Supplementary Fig. 12, we show the effects of including an ad hoc static mean-field + U term on the Ru sites in DFT calculations. Adding such a phenomenological term to the Kohn-Sham Hamiltonian shifts the bands relative to each other (up/down in energy) so as to force the orbital occupancies towards integer fillings, rather than also shrinking the bandwidths of the quasiparticle excitations, as would occur in a more realistic

Supplementary Table I. Crystal structures used in DFT simulations (all units of length are given in Å)

Name	Space group	a_{rutile}	b_{rutile}	c_{rutile}	$d_{1\bar{1}0}$	d_{110}	Ru - apical O bond length(s)	Ru - equatorial O bond length(s)
bulk RuO ₂ - expt.	#136	4.492	4.492	3.106	3.176	3.176	1.941	1.984
bulk RuO ₂ - DFT	#136	4.517	4.517	3.130	3.194	3.194	1.945	2.002
RuO ₂ (110) - DFT	#65	4.606	4.606	2.982	3.266	3.249	1.946, 1.957	1.980, 1.984
RuO ₂ (101) - DFT	#58	4.525	4.618	3.101	3.233	3.233	1.969	2.000

Supplementary Figure 12. Strain dependence of the electronic structure of RuO₂, according to DFT (+ U).

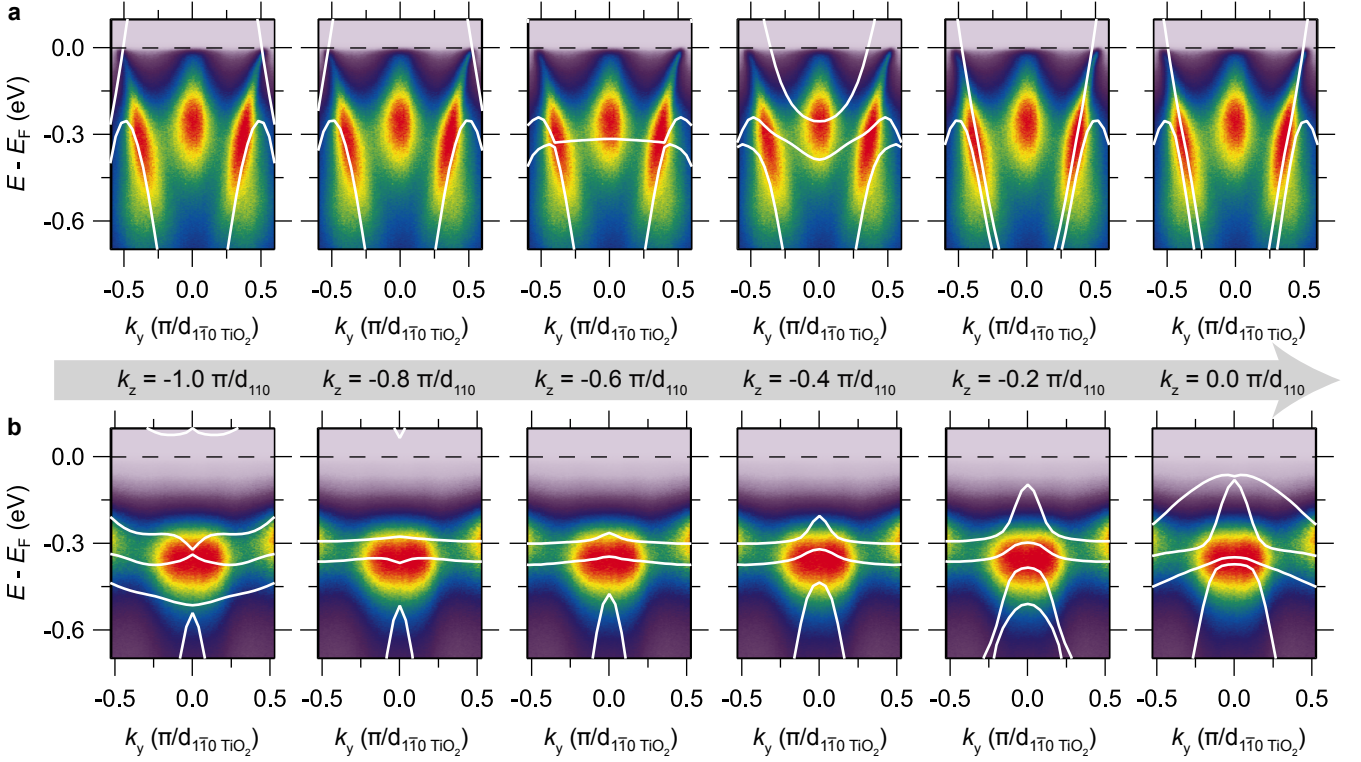
theory that includes dynamical electron-electron interactions. The blue and red traces are reproduced from the non-magnetic DFT + U ($U = 2$ eV) results presented in Fig. 4a of the main text; the purple and orange traces are the results of repeating GGA + SOC calculations for the same RuO₂(110) and bulk RuO₂ crystal structures, respectively, but now setting $U = 0$. Irrespective of U , both sets of calculations show a shift of the $d_{||}$ -derived flat bands towards E_F and concomitant enhancement of the density of states (DOS) near E_F when the amount of c -axis compression is increased upon going from bulk RuO₂ to RuO₂(110), as indicated by the gray arrows. While these strain-dependent trends in the electronic structure are robust against fine-tuning of parameters employed in the calculations, Supplementary Fig. 12 also suggests that the calculated positions of the peaks in the DOS and the exact values of the DOS near E_F should not be taken too seriously, as there are considerable theoretical uncertainties in these quantities, depending on the choice of U . We leave a complete treatment of the effects on the electronic structure of commensurate $\mathbf{Q}_{\text{AFM}} = (100)$ antiferromagnetic spin-density wave order [13, 37] to future studies [38], because it is not possible in standard DFT-based approaches to stabilize self-consistent solutions for the spin densities that have small values of the ordered

magnetic moment comparable to those measured experimentally ($\approx 0.05 \mu_B/\text{Ru}$) [13].

Supplementary Note 6: DETERMINATION OF OUT-OF-PLANE MOMENTA PROBED BY ANGLE RESOLVED PHOTOEMISSION SPECTROSCOPY

Figure 3d-f of the main text compares the electronic structure of a 7 nm thick RuO₂/TiO₂(110) sample experimentally measured by angle-resolved photoemission spectroscopy (ARPES) with the results of DFT + U simulations. To make this comparison, it is necessary to determine what range of out-of-plane momenta $k_z = k_{110}$ in the initial state are probed by ARPES at a given final-state kinetic energy and momentum. This was established by plotting the DFT-computed $E(\mathbf{k})$ dispersions on top of the experimentally measured spectra along several one-dimensional cuts through momentum space measured over a small range of kinetic energies corresponding to near- E_F states at the given photon energy (21.2 eV), and allowing k_z to vary in the calculations so as to best match the experimental data.

Supplementary Fig. 13 shows representative examples of this procedure for experimental spectra taken along



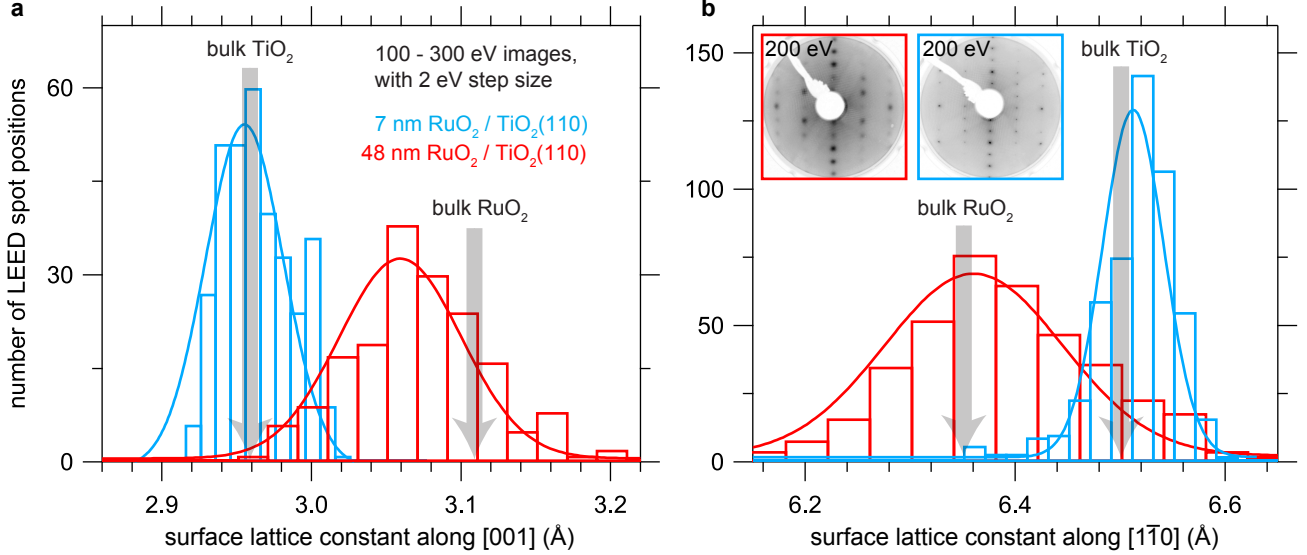
Supplementary Figure 13. **Determination of k_z probed by ARPES for $\text{RuO}_2(110)$.** Experimental ARPES spectra for a 7 nm thick $\text{RuO}_2/\text{TiO}_2(110)$ sample reproduced from **a**, Fig. 3f and **b**, Fig. 3e of the main text, overlaid with the band dispersions from DFT + U ($U = 2$ eV) calculations in white. For the data in **a**, $k_x = k_{001}$ is fixed at zero and in **b**, $k_x = \pi/c$. Moving from left to right, k_z is incremented in the DFT simulations in steps of $0.2 \pi/d_{110}$ starting from $-1.0 \pi/d_{110}$.

the one-dimensional cuts shown in Fig. 3f (top row, $k_x = k_{001}$ fixed at zero) and in Fig. 3e (bottom row, $k_x = \pi/c$) of the main text. Moving from left to right, k_z is incremented in the DFT simulations in steps of $0.2 \pi/d_{110}$ starting from $-1.0 \pi/d_{110}$. For the panels in Supplementary Fig. 13a, the k_{FS} and electron-like character of the band crossing E_F are best fitted by calculations with k_z in the range $-0.2 \rightarrow 0.0 \pi/d_{110}$. Likewise, for the panels in Supplementary Fig. 13b, k_z values in the range $-0.6 \rightarrow -0.3 \pi/d_{110}$ best reproduce the measured spectra, although the results here are more ambiguous because of the insensitivity of the flat-band energies to the precise value of k_{110} . Therefore, we took the range of reduced initial-state out-of-plane momenta probed at normal emission ($k_x = k_y = 0$) to be $k_{z,i} = -0.1 \pm 0.1 \pi/d_{110}$. Assuming a free-electron-like model of final states, the final-state $k_{z,f}$ is given by the expression

$$k_{z,f} = \sqrt{\frac{2m_e(E_k \cos^2 \theta + V_0)}{\hbar^2}} = \frac{2\pi}{2d_{110}}N + k_{z,i}, \quad (7)$$

where m_e is the free-electron mass, E_k is the kinetic energy of the photoelectrons, θ is the emission angle relative to the surface normal, V_0 is the inner potential,

and $2d_{110}$ is the spacing between equivalent lattice points along the out-of-plane direction (N can adopt any integer value). Substituting $E_k = 16.6 \pm 0.3$ eV, $\theta = 0^\circ$, $k_{z,i} = -0.1 \pm 0.1 \pi/d_{110}$, and $d_{110} = 3.23$ Å into Supplementary Eq. (7), we find that an inner potential of 13.7 ± 2.3 eV is compatible with our determination of $k_{z,i}$. Taking this same value of V_0 and setting $\theta = 30-35^\circ$ in Supplementary Eq. (7)—as is appropriate for the experimental data in the panels displayed in Supplementary Fig. 13b—yields $k_{z,i} = -0.35 \pm 0.17 \pi/d_{110}$; visual inspection of the DFT bands for this range of $k_{z,i}$ show that the calculations also reproduce the experimental spectrum reasonably well in this region of the Brillouin zone. The curved green planes drawn in the Brillouin zone schematic in Fig. 3c of the main text are constructed by evaluating Supplementary Eq. (7) with $V_0 = 13.7$ eV and $N = 3$ for all (k_x, k_y) , and accounting for an intrinsic uncertainty of $\approx 0.2 \pi/d_{110}$ in k_z owing to the finite elastic escape depth of photoelectrons, which we take to be ≈ 5 Å.



Supplementary Figure 14. **Surface lattice constant refinement by LEED spot position analysis.** Results are shown for two $\text{RuO}_2(110)$ films of different thicknesses, 7 nm (blue) and 48 nm (red). The histograms in panels **a** and **b** summarize the measured values for c and $2d_{1\bar{1}0}$, respectively. For reference, the gray arrows indicate the lattice parameters expected for a commensurately strained film (bulk TiO_2) and a fully strain-relaxed film (bulk RuO_2).

Supplementary Note 7: SURFACE LATTICE CONSTANT REFINEMENT

In Supplementary Fig. 14, we present the results of a surface lattice constant refinement for two different $\text{RuO}_2/\text{TiO}_2(110)$ films of different thicknesses, 7 nm and 48 nm. For both samples we acquired many low-energy electron diffraction (LEED) images at normal incidence using incident energies ranging from $E = 100 - 300$ eV in 2 eV steps; for examples of the raw data, the insets in Supplementary Fig. 14b contain representative images taken at 200 eV. For each image, we located the positions of all visible spots and indexed the spots according to their in-plane momentum transfer values $\mathbf{q}_{\parallel} = 2\pi(H/c, K/2d_{1\bar{1}0})$, where H and K are integers and, by our convention, H defines the magnitude of \mathbf{q}_{\parallel} along $[001]$ (nearly horizontal in the images in Supplementary Fig. 14), and K defines the magnitude of \mathbf{q}_{\parallel} along $[1\bar{1}0]$ (nearly vertical). We then calculated the distance of all spots from the specular $\mathbf{q}_{\parallel} = (0, 0)$ reflection and converted these image distances D (in pixel space) to scattering angles $\sin(\theta)$ (where θ is the angle of each diffracted electron beam relative to the surface normal) based on $D \rightarrow \sin(\theta)$ calibrations that were independently determined from reference measurements on $\text{SrTiO}_3(001)$ surfaces having a known lattice constant. Note that these calibrations absorb the overall scaling factor that depends on the working distance between the LEED screen and the sample (and the camera image magnification factor), as well as some higher-order distortions of the spot patterns that result from the sample

not being positioned precisely at the center of curvature of the LEED screen (and the screen itself being slightly aspherical).

From these values of $\sin(\theta)$, the electron energies E at which each LEED pattern was recorded, and the (H, K) indices, we compiled lists of lattice constants corresponding to each fitted spot position. For simplicity in analysis, we restricted our attention to spots having \mathbf{q}_{\parallel} purely aligned with $[001]$ or $[1\bar{1}0]$. Elastic scattering and conservation of momentum modulo translations of the surface reciprocal lattice together require that:

$$|\mathbf{q}_{\parallel}| = k \sin(\theta) = \sqrt{2m_e E} \sin(\theta) / \hbar, \quad (8)$$

which for Bragg spots of the type $\mathbf{q}_{\parallel} = 2\pi(H/c, 0)$ and $2\pi(0, K/2d_{1\bar{1}0})$, reduces to:

$$c = \frac{2\pi\hbar H}{\sqrt{2m_e E} \sin(\theta)} \quad \text{and} \quad 2d_{1\bar{1}0} = \frac{2\pi\hbar K}{\sqrt{2m_e E} \sin(\theta)}. \quad (9)$$

Here c and $2d_{1\bar{1}0}$ are the surface lattice constants along $[001]$ and $[1\bar{1}0]$ that are expected for an unreconstructed (110) -oriented rutile surface. Histograms of the values obtained in this way for c are displayed in Supplementary Fig. 14a, and the results for $2d_{1\bar{1}0}$ are displayed in Supplementary Fig. 14b. For reference, we also indicate by gray arrows the surface lattice constants expected for bulk-terminated TiO_2 ($c = 2.96$ Å, $2d_{1\bar{1}0} = 6.50$ Å) and bulk-terminated RuO_2 ($c = 3.11$ Å, $2d_{1\bar{1}0} = 6.35$ Å). The surface lattice constants for the 7 nm thick $\text{RuO}_2(110)$ sample in blue, ($c = 2.96 \pm 0.03$ Å, $2d_{1\bar{1}0} = 6.51 \pm 0.05$ Å),

match those of TiO_2 within the $\approx 1.0\%$ resolution of the measurements, indicating that this film is (nearly) commensurately strained to the substrate along both $[001]$ and $[\bar{1}\bar{1}0]$. By contrast, the 48 nm thick $\text{RuO}_2(110)$ sample in red shows broader LEED spots, indicating lower surface crystallinity than the 7 nm thick sample, which results in wider distributions of the extracted lattice constants. Furthermore, the centers of mass of the red distributions, ($c = 3.07 \pm 0.06 \text{ \AA}$, $2d_{\bar{1}\bar{1}0} = 6.39 \pm 0.11 \text{ \AA}$), are displaced away from the blue distributions towards the values expected for bulk RuO_2 ; this is why in Fig. 4b-c of the main text we suggest that the surface electronic structure of this 48 nm thick sample measured by ARPES—which probes the film over a comparable depth to LEED, within $< 1 \text{ nm}$ from the top film surface—should be more representative of bulk RuO_2 .

Supplementary Note 8: EXTRACTING THE NEAR- E_F DENSITY OF STATES FROM ARPES MEASUREMENTS

In Supplementary Fig. 15 we present LEED and ARPES data taken on three different RuO_2 thin-film samples: 19 nm thick $\text{RuO}_2(101)$, 7 nm thick $\text{RuO}_2(110)$, and 48 nm thick $\text{RuO}_2(110)$. In Supplementary Fig. 15a, all of the samples show LEED spot patterns with the periodicities expected for unreconstructed (101)- and (110)-oriented rutile surfaces, respectively; furthermore, the sharpness of the patterns suggest high degrees of surface crystallinity, such that in-plane momentum should be a nearly conserved parameter in photoemission. Given that strained $\text{RuO}_2(110)$ samples superconduct at measurable T_c s, while $\text{RuO}_2(101)$ samples and bulk RuO_2 do not, the question we wanted to address using ARPES was: how does the density of states near the Fermi level, $N(E_F)$, evolve between these samples? Recall that based on the LEED lattice constant analysis described in Supplementary Fig. 14, most of the substrate-imposed epitaxial strains are relaxed at the top surface of the 48 nm thick $\text{RuO}_2(110)$ sample, such that its electronic structure probed by ARPES is a reasonable proxy for that of bulk RuO_2 . Specifically, the quantity of interest as it relates to the low-energy physics is:

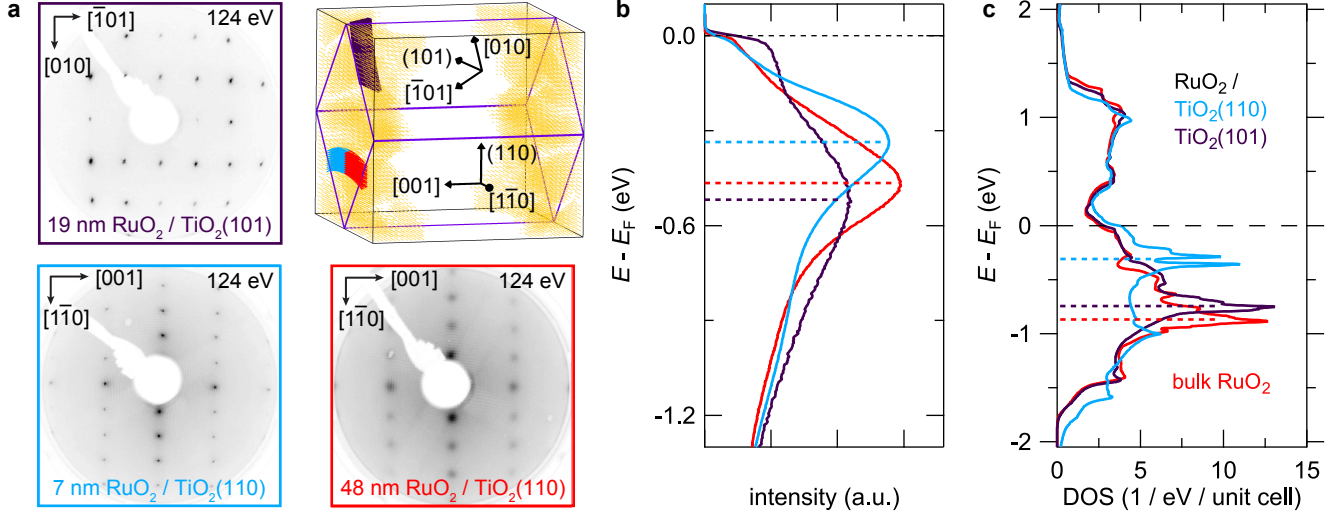
$$N(E_F) \propto \int_{E_F-\delta}^{E_F+\delta} \int_{\text{BZ}} A(\mathbf{k}, \omega) d\mathbf{k} d\omega, \quad (10)$$

where $A(\mathbf{k}, \omega)$ is the single-particle spectral function, integrated over all momenta \mathbf{k} in the Brillouin zone (BZ) and over some limited range of energies ω near E_F (δ is some small parameter).

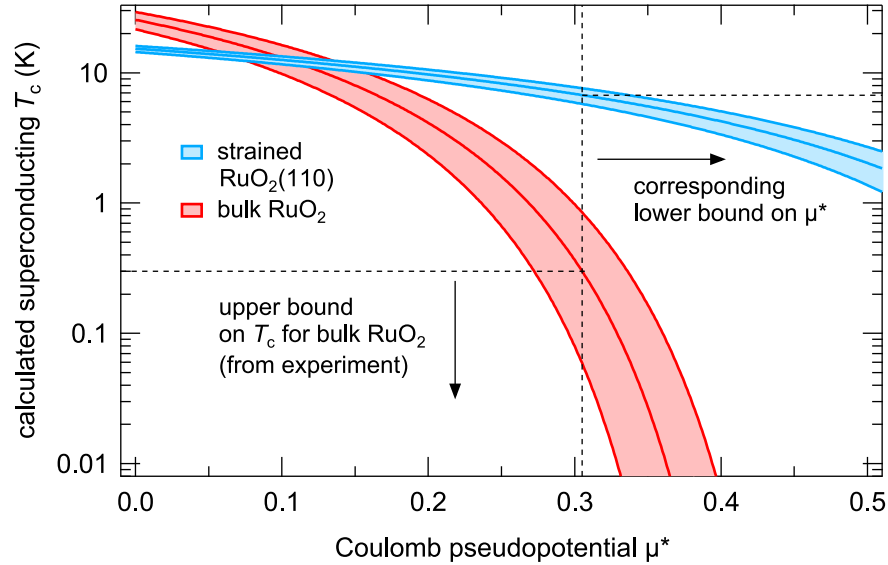
Two separate factors make it extremely challenging to quantitatively extract the total $N(E_F)$ directly from data taken with our lab-based ARPES system. First, our inability to continuously vary the photon energy—or equivalently, the kinetic energy of the photoelectrons at E_F —implies that only regions of the Brillouin zone with

specific k_z can be probed, cf. Supplementary Eq. (7). Therefore the full integration over \mathbf{k} in Supplementary Eq. (10) cannot be performed using a lab-based ARPES setup, which is especially problematic in a material such as RuO_2 that has a highly three-dimensional electronic structure depending strongly on k_z (cf. Supplementary Fig. 13). Second, even if the entire Brillouin zone could be mapped exhaustively, the intensity measured in ARPES is not the initial-state spectral function $A(\mathbf{k}, \omega)$, but rather this quantity multiplied by probabilities (i.e., matrix elements) for photoemission, which are difficult to account for theoretically.

With these qualifications in mind, there is a route to answering the simpler question of whether $N(E_F)$ increases in strained $\text{RuO}_2(110)$ compared with strained $\text{RuO}_2(101)$ or bulk RuO_2 : we simply need to determine where the flat bands with d_{\parallel} orbital character are located in energy relative to E_F . DFT calculations suggest that if these bands move closer to (further away from) E_F , the total $N(E_F)$ will increase (decrease), respectively. To approximately determine the positions of these bands experimentally, we integrated the photoemission intensity over the color-coded slabs in the Brillouin zone schematic in Supplementary Fig. 15a, plotted the resulting energy distribution curves (EDCs) in Supplementary Fig. 15b, and found the maxima in the EDCs as indicated by the dashed lines. The regions colored yellow in the Brillouin zone denote where the near- E_F wavefunctions have greater than 90% d_{\parallel} orbital character, according to our DFT + Wannier90 calculations; since all slabs lie in this region, we expect that the dominant contributions to the measured EDCs are from d_{\parallel} initial states. Note that the region of $k_z = k_{110}$ probed by ARPES with He-I α (21.2 eV) photons on the (110)-oriented samples is well-constrained by analysis of the $E(\mathbf{k})$ dispersions as outlined in Supplementary Fig. 13; however, for the (101)-oriented sample the region of $k_z = k_{101}$ probed by ARPES with He-II α (40.8 eV) photons is merely calculated from the free-electron final state model in Supplementary Eq. (7), using the same inner potential as for $\text{RuO}_2(110)$, and thus is subject to greater experimental uncertainties. Nonetheless, the results of this analysis qualitatively agree with the strain-dependent trends anticipated by DFT (Supplementary Fig. 15c): in highly strained $\text{RuO}_2(110)$ films (blue), the flat bands move closer to E_F compared with either more strain-relaxed $\text{RuO}_2(110)$ films (red) or commensurately strained $\text{RuO}_2(101)$ films (purple). This modification of the effective d orbital degeneracies boosts $N(E_F)$, which—as proposed in the main text—likely contributes to the enhanced superconducting T_c s observed in highly strained $\text{RuO}_2(110)$ samples.



Supplementary Figure 15. **Strain dependence of the near- E_F density of states.** **a**, LEED patterns recorded at 124 eV for a 19 nm thick $\text{RuO}_2(101)$, a 7 nm thick $\text{RuO}_2(110)$, and a 48 nm thick $\text{RuO}_2(110)$ sample, along with a schematic of the Brillouin zone showing the regions of \mathbf{k} -space over which we integrated the ARPES data for these samples to obtain the average energy distribution curves shown in **b**. Regions of the Brillouin zone shaded yellow indicate where the near- E_F Kohn-Sham wavefunctions have $> 90\%$ $d_{||}$ orbital character. **b**, The colored dashed lines represent the peak positions of the energy distribution curves. By locating the $d_{||}$ -derived flat bands in this way, trends in how $N(E_F)$ evolves with strain can be more reliably extracted from ARPES data than by directly reading off the measured photoemission intensity at E_F . **c**, Strain-dependent changes in the total DOS expected according to DFT + U simulations, reproduced from Fig. 4a.



Supplementary Figure 16. **Calculated T_c s for bulk RuO_2 and strained $\text{RuO}_2(110)$, assuming an electron-phonon mediated mechanism of superconductivity.** T_c is evaluated from Supplementary Eq. (11) using DFT-based calculations of $\lambda_{\text{el-ph}}$ and ω_{log} , and allowing μ^* to vary. As indicated by the vertical and horizontal dashed lines, $\mu^* > 0.30$ is the region of parameter space consistent with the reported non-superconducting behavior of bulk RuO_2 ($T_c < 0.3$ K [39]), which in turn places an upper bound ($T_c < 7$ K) on the strain-enhanced T_c s expected for $\text{RuO}_2(110)$. Shaded regions indicate the changes in T_c that would result from $\pm 10\%$ errors in the calculated values of $\lambda_{\text{el-ph}}$.

Supplementary Note 9: MIGDAL-ELIASHBERG CALCULATIONS OF T_c

As described in the Methods section of the main text, we performed first-principles DFT-based electron-phonon coupling calculations of the isotropic Eliashberg spectral function $\alpha^2F(\omega)$ and total electron-phonon coupling constant $\lambda_{\text{el-ph}}$ (integrated over all phonon modes and wavevectors) for bulk RuO₂ and commensurately strained RuO₂(110). From these quantities, we estimated the superconducting transition temperatures using the semi-empirical McMillan-Allen-Dynes formula:

$$T_c = \frac{\omega_{\text{log}}}{1.2} \exp \left[-\frac{1.04(1 + \lambda_{\text{el-ph}})}{\lambda_{\text{el-ph}} - \mu^*(1 + 0.62\lambda_{\text{el-ph}})} \right] \quad (11)$$

McMillan obtained a formula resembling Supplementary Eq. (11) by numerically solving the equations of finite-temperature Migdal-Eliashberg theory using the experimentally measured spectral function of niobium [40]; Allen and Dynes improved the agreement of McMillan's formula with experimentally measured $\alpha^2F(\omega)$ and T_c s for a variety of conventional superconductors by introducing an appropriately weighted average over $\alpha^2F(\omega)$ in the prefactor of the exponential, rather than using the Debye temperature [41]. In essence, Supplementary Eq. (11) can be considered an extension of Eq. (1) from the main text that identifies phonons as the bosonic modes that mediate Cooper pairing (i.e., $\lambda = \lambda_{\text{el-ph}}$), and which remains valid even in the limit of stronger couplings (i.e., $\lambda > 1$) by virtue of Migdal's theorem for the electron-phonon interaction.

For bulk RuO₂ (strained RuO₂(110), respectively), we obtained $\lambda_{\text{el-ph}} = 0.685$ and $\omega_{\text{log}} = 34.1$ meV ($\lambda_{\text{el-ph}} = 1.97$ and $\omega_{\text{log}} = 7.59$ meV). The large strain-induced enhancement in $\lambda_{\text{el-ph}}$ and shift of ω_{log} to lower frequencies is caused by substantial phonon softening that occurs under *c*-axis compression in the rutile structure. In fact, we found that some of the calculated zone-boundary phonon frequencies even become imaginary under strain in RuO₂(110), possibly indicating an incipient structural instability. A more detailed account of this phenomenon will be described in a future publication; for the purposes of this work, we omitted such phonon modes in subsequent electron-phonon coupling calculations, and neglected any errors this may cause in $\lambda_{\text{el-ph}}$ and ω_{log} .

To convert the calculated values of $\lambda_{\text{el-ph}}$ and ω_{log} to T_c s via Supplementary Eq. (11) requires knowledge of the appropriate value(s) of the screened Coulomb interaction μ^* between quasiparticles. Typically μ^* is chosen in an ad hoc fashion to match the experimentally measured T_c of a given material. Because bulk RuO₂ is not known to be superconducting at experimentally accessible temperatures, we cannot employ such a prescription here; nevertheless, we can use the experimentally measured least upper bound on T_c for bulk RuO₂ ($T_c < 0.3$ K [39]) to

place a lower bound on μ^* ($\mu^* > 0.30$), as illustrated by the dashed lines in Supplementary Fig. 16. For this range of μ^* , inserting the values of $\lambda_{\text{el-ph}}$ and ω_{log} calculated for RuO₂(110) into Supplementary Eq. (11) predicts $T_c < 7$ K, which agrees reasonably well with the experimentally measured values. Because several uncontrolled approximations enter into these estimates of T_c , we consider this level of agreement as suggestive, although not conclusive, evidence for a phonon-mediated mechanism of superconductivity; in any case, it is clear that reducing the axial ratio *c/a* in appropriately strained variants of RuO₂ robustly boosts $\lambda_{\text{el-ph}}$, in good agreement with expectations based on steric trends for other rutile compounds [42, 43]. Any effects of strain on μ^* are ignored for the purposes of this work.

- [1] Miccoli, I., Edler, F., Pfner, H. & Tegenkamp, C. The 100th anniversary of the four-point probe technique: the role of probe geometries in isotropic and anisotropic systems. *Journal of Physics: Condensed Matter* **27**, 223201 (2015).
- [2] Ryden, W. D., Lawson, A. W. & Sartain, C. C. Electrical Transport Properties of IrO₂ and RuO₂. *Physical Review B* **1**, 1494–1500 (1970).
- [3] Glassford, K. M. & Chelikowsky, J. R. Electron transport properties in RuO₂ rutile. *Physical Review B* **49**, 7107–7114 (1994).
- [4] Wolff, K. *et al.* Influence of the vicinal substrate miscut on the anisotropic two-dimensional electronic transport in Al₂O₃–SrTiO₃ heterostructures. *Journal of Applied Physics* **128**, 085302 (2020).
- [5] Wu, J. *et al.* Electronic nematicity in Sr₂RuO₄. *Proceedings of the National Academy of Sciences* **117**, 10654–10659 (2020).
- [6] Schneider, C. W., Thiel, S., Hammerl, G., Richter, C. & Mannhart, J. Microlithography of electron gases formed at interfaces in oxide heterostructures. *Applied Physics Letters* **89**, 122101 (2006).
- [7] Hsu, J. W. P. & Kapitulnik, A. Superconducting transition, fluctuation, and vortex motion in a two-dimensional single-crystal Nb film. *Physical Review B* **45**, 4819–4835 (1992).
- [8] Kim, M., Kozuka, Y., Bell, C., Hikita, Y. & Hwang, H. Y. Intrinsic spin-orbit coupling in superconducting δ -doped SrTiO₃ heterostructures. *Physical Review B* **86**, 085121 (2012).
- [9] Werthamer, N. R., Helfand, E. & Hohenberg, P. C. Temperature and Purity Dependence of the Superconducting Critical Field, H_{c2}. III. Electron Spin and Spin-Orbit Effects. *Physical Review* **147**, 295–302 (1966).
- [10] Wissberg, S. & Kalisky, B. Large-scale modulation in the superconducting properties of thin films due to domains in the SrTiO₃ substrate. *Physical Review B* **95**, 144510 (2017).
- [11] Kalisky, B. *et al.* Stripes of increased diamagnetic susceptibility in underdoped superconducting Ba(Fe_{1-x}Co_x)₂As₂ single crystals: Evidence for an enhanced superfluid density at twin boundaries. *Physical Review B* **81**, 184513 (2010).
- [12] Kalisky, B. *et al.* Behavior of vortices near twin boundaries in underdoped Ba(Fe_{1-x}Co_x)₂As₂. *Physical Review B* **83**, 064511 (2011).
- [13] Berlijn, T. *et al.* Itinerant Antiferromagnetism in RuO₂. *Physical Review Letters* **118**, 077201 (2017).
- [14] Burdett, J. K., Hughbanks, T., Miller, G. J., Richardson, J. W. & Smith, J. V. Structural-electronic relationships in inorganic solids: powder neutron diffraction studies of the rutile and anatase polymorphs of titanium dioxide at 15 and 295 K. *Journal of the American Chemical Society* **109**, 3639–3646 (1987).
- [15] Miceli, P. F. & Palmstrom, C. J. X-ray scattering from rotational disorder in epitaxial films: An unconventional mosaic crystal. *Physical Review B* **51**, 5506–5509 (1995).
- [16] Miceli, P. F., Weatherwax, J., Krentsel, T. & Palmstrom, C. J. Specular and diffuse reflectivity from thin films containing misfit dislocations. *Physica B: Condensed Matter* **221**, 230–234 (1996).
- [17] Kortan, A. R., Hong, M., Kwo, J., Mannaerts, J. P. & Kopylov, N. Structure of epitaxial Gd₂O₃ films grown on GaAs(100). *Physical Review B* **60**, 10913–10918 (1999).
- [18] Barabash, R. I., Donner, W. & Dosch, H. X-ray scattering from misfit dislocations in heteroepitaxial films: The case of Nb(110) on Al₂O₃. *Applied Physics Letters* **78**, 443–445 (2001).
- [19] Biegalski, M. D. *et al.* Critical thickness of high structural quality SrTiO₃ films grown on orthorhombic (101) DyScO₃. *Journal of Applied Physics* **104**, 114109 (2008).
- [20] Wang, T., Ganguly, K., Marshall, P., Xu, P. & Jalan, B. Critical thickness and strain relaxation in molecular beam epitaxy-grown SrTiO₃ films. *Applied Physics Letters* **103**, 212904 (2013).
- [21] Kaganer, V. M., Koehler, R., Schmidbauer, M., Opitz, R. & Jenichen, B. X-ray diffraction peaks due to misfit dislocations in heteroepitaxial structures. *Physical Review B* **55**, 1793–1810 (1997).
- [22] Csizsar, S. I. & Tjeng, L. H. *X-ray diffraction and X-ray absorption of strained CoO and MnO thin films*. Ph.D. thesis, University of Groningen (2005).
- [23] Xie, S. *et al.* Coherent, atomically thin transition-metal dichalcogenide superlattices with engineered strain. *Science* **359**, 1131–1136 (2018).
- [24] Bachmann, M. D. *et al.* Spatial control of heavy-fermion superconductivity in CeIrIn₅. *Science* **366**, 221–226 (2019).
- [25] Warusawithana, M. P. *et al.* A Ferroelectric Oxide Made Directly on Silicon. *Science* **324**, 367–370 (2009).
- [26] Glatz, A., Aranson, I. S., Baturina, T. I., Chitchev, N. M. & Vinokur, V. M. Self-organized superconducting textures in thin films. *Physical Review B* **84**, 024508 (2011).
- [27] Eley, S., Gopalakrishnan, S., Goldbart, P. M. & Mason, N. Approaching zero-temperature metallic states in mesoscopic superconductor–normal–superconductor arrays. *Nature Physics* **8**, 59–62 (2012).
- [28] Pinto, N. *et al.* Dimensional crossover and incipient quantum size effects in superconducting niobium nanofilms. *Scientific Reports* **8**, 4710 (2018).
- [29] Meyer, T. L., Jiang, L., Park, S., Egami, T. & Lee, H. N. Strain-relaxation and critical thickness of epitaxial La_{1.85}Sr_{0.15}CuO₄ films. *APL Materials* **3**, 126102 (2015).
- [30] Kapitulnik, A., Kivelson, S. A. & Spivak, B. Colloquium: Anomalous metals: Failed superconductors. *Reviews of Modern Physics* **91**, 011002 (2019).
- [31] Haviland, D. B., Liu, Y. & Goldman, A. M. Onset of superconductivity in the two-dimensional limit. *Physical Review Letters* **62**, 2180–2183 (1989).
- [32] Jaeger, H. M., Haviland, D. B., Orr, B. G. & Goldman, A. M. Onset of superconductivity in ultrathin granular metal films. *Physical Review B* **40**, 182–196 (1989).
- [33] Steiner, M. A., Breznay, N. P. & Kapitulnik, A. Approach to a superconductor-to-Bose-insulator transition in disordered films. *Physical Review B* **77**, 212501 (2008).
- [34] Mackenzie, A. P. *et al.* Extremely Strong Dependence of Superconductivity on Disorder in Sr₂RuO₄. *Physical Review Letters* **80**, 161–164 (1998).
- [35] Kresse, G. & Furthmüller, J. Efficient iterative schemes for ab initio total-energy calculations using a plane-wave basis set. *Physical Review B* **54**, 11169–11186 (1996).

- [36] Kresse, G. & Joubert, D. From ultrasoft pseudopotentials to the projector augmented-wave method. *Physical Review B* **59**, 1758–1775 (1999).
- [37] Zhu, Z. *et al.* Anomalous Antiferromagnetism in Metallic RuO₂ Determined by Resonant X-ray Scattering. *Physical Review Letters* **122**, 017202 (2019).
- [38] Ahn, K.-H., Hariki, A., Lee, K.-W. & Kunes, J. Antiferromagnetism in RuO₂ as *d*-wave Pomeranchuk instability. *Physical Review B* **99**, 184432 (2019).
- [39] Lin, J. J. *et al.* Low temperature electrical transport properties of RuO₂ and IrO₂ single crystals. *Journal of Physics: Condensed Matter* **16**, 8035 (2004).
- [40] McMillan, W. L. Transition Temperature of Strong-Coupled Superconductors. *Physical Review* **167**, 331–344 (1968).
- [41] Allen, P. B. & Dynes, R. C. Transition temperature of strong-coupled superconductors reanalyzed. *Physical Review B* **12**, 905–922 (1975).
- [42] Eyert, V. The metal-insulator transitions of VO₂: A band theoretical approach. *Annalen der Physik* **11**, 650–704 (2002).
- [43] Hiroi, Z. Structural instability of the rutile compounds and its relevance to the metal-insulator transition of VO₂. *Progress in Solid State Chemistry* **43**, 47–69 (2015).